CORROSION AND HYDROGEN EMBRITTLEMENT OF NANOCRYSTALLINE NICKEL

by

TAPAS DESAI

Presented to the Faculty of the Graduate School of
The University of Texas at Arlington in Partial Fulfillment
of the Requirements
for the Degree of

MASTER OF SCIENCE IN MATERIALS SCIENCE AND ENGINEERING

THE UNIVERSITY OF TEXAS AT ARLINGTON
MAY 2013

ACKNOWLEDGEMENTS

I would like to express my gratitude to Dr. E. I. Meletis for his valuable guidance, support and contribution to my research.

I also want to thank my research group, who has helped me throughout my research project in countless ways. I especially appreciate the help of Jessica Mooney and Adam Smith for helping me through the sputter deposition and mechanical testing parts of my research. I am thankful to Dr. Y.W. Hao and his research group for their help with the electrochemical hydrogen charging cell. I also am grateful to have a caring and supportive family, without whom, I would not have had this opportunity.

I also appreciate the time and consideration of my committee members and Ms. Jennifer Standlee, for her patience and support.

May 3rd, 2013

ABSTRACT

CORROSION AND HYDROGEN EMBRITTLEMENT OF NANOCRYSTALLINE NICKEL

Tapas Desai, M.Sc.

The University of Texas at Arlington, 2013

Supervising Professor: Efstathios I. Meletis

Nanocrystalline (nc) materials have attracted the interest of the scientific community because of their unique physical and mechanical properties. However, limited research has been performed to analyze their electrochemical behavior. The majority of research in the field of electrochemical and corrosion behavior exists for electrodeposited nanocrystalline metals.

This research studies the behavior of sputter-deposited nc Nickel films in corrosive and hydrogen environment by potentiodynamic polarization and microindentation. The surface morphology and composition of the samples was examined by Scanning Electron Microscopy and Energy Dispersive X-Ray spectroscopy. Bulk Ni samples exhibit mild passivation in 3.5 % NaCl solution. The surface reveals a fine distribution of small pits and numerous large pits. However, nc Ni films show a higher corrosion potential, but lower corrosion rate. This can be attributed to the rapid formation of a passive film to resist the corrosion, and better purity of sputtered films. A very uniform and periodic corrosion pattern is observed on the surface, without any pitting. In 0.1 N H_2SO_4 solution, active dissolution of Ni was observed in both bulk and nanocrystalline samples. This is due to the absence of passivation for Ni in this

environment. Nc Ni shows a higher corrosion rate and higher anodic corrosion potential. This behavior is attributed to a higher density of grain boundaries that act as a catalyst to the hydrogen reduction reaction and increase the corrosion rate.

Effect of electrochemically charged hydrogen was observed for bulk and nanocrystalline Nickel. Bulk Ni displayed a slight increase in hardness and signs of hydrogen induced plastic deformation. On the other hand, the nanocrystalline Ni shows brittle failure by buckling and spalling. This is attributed to its limited ductility and the high density that act as preferred sites for hydrogen adsorption and subsequently enhance hydrogen diffusion, leading to embrittlement.

TABLE OF CONTENTS

LIST OF ILLUSTRATIONS

LIST OF TABLES

CHAPTER 1

INTRODUCTION

Due to considerable grain size reduction and large volume fraction of grain boundaries and triple junctions, nc materials have physical, mechanical and electrochemical properties that differ from their conventional counterparts. Even as the mechanical, electrical and magnetic properties of such nc materials have been the focus of popular research [1] [2], electrochemical properties such as corrosion and hydrogen embrittlement remain relatively unexplored.

Corrosion is caused by electrochemical reactions between a material and its environment and it results in deterioration of the material. Uniform corrosion can be visually seen and predicted in materials that lack corrosion resistance. However in passive materials, like Nickel, corrosion is more localized and intergranular. This is difficult to notice visually, far more difficult to predict and can cause catastrophic failure of components. Nanocrystalline (nc) materials have a higher volume fraction of grain boundaries, which might lead to more active sites for corrosion. However, as grain boundaries in nc materials are well spread out, the corrosion might not be as dangerous as it is not localized [3].

Hydrogen Embrittlement (HE) is a severe problem that degrades material properties. This problem affects several high strength metals like steels and Nickel alloys but has not been fully understood. Hydrogen embrittlement is caused by the ingress of hydrogen in a material at critical points, like triple junctions and grain boundaries [4]. The diffusion of hydrogen is too rapid to be stopped. And once a material is affected by hydrogen, it is very difficult and sometimes impossible to reverse it. Hydrogen Embrittlement is manifested by a sudden loss in ductility, strength and toughness. Through several studies involving high resolution fractography and *in-situ* TEM, researchers have established that Hydrogen Enhanced Localized Plasticity (HELP) and Hydrogen Enhanced Decohesion (HEDE) are viable mechanisms for failure by hydrogen embrittlement. However, the crack propagation varied between intergranular, transgranular and mixed mode [5].

Nanocrystalline Nickel has better mechanical and electrical properties as compared to its bulk counterpart. These properties are exploited in precision engineering applications like microchip production and components for microelectromechanical (MEMS) devices. Nanocrystalline Nickel is electroplated in small volumes onto micro scale components for MEMS devices. It is preferred over other materials as it can be electroplated at lower temperatures. On the other hand, polysilicon requires an annealing treatment, which would damage other electronic components on the assembly. For precision electroplating of a material, the LIGA (Lithographae Galvanoformung Abformung) technique is used.

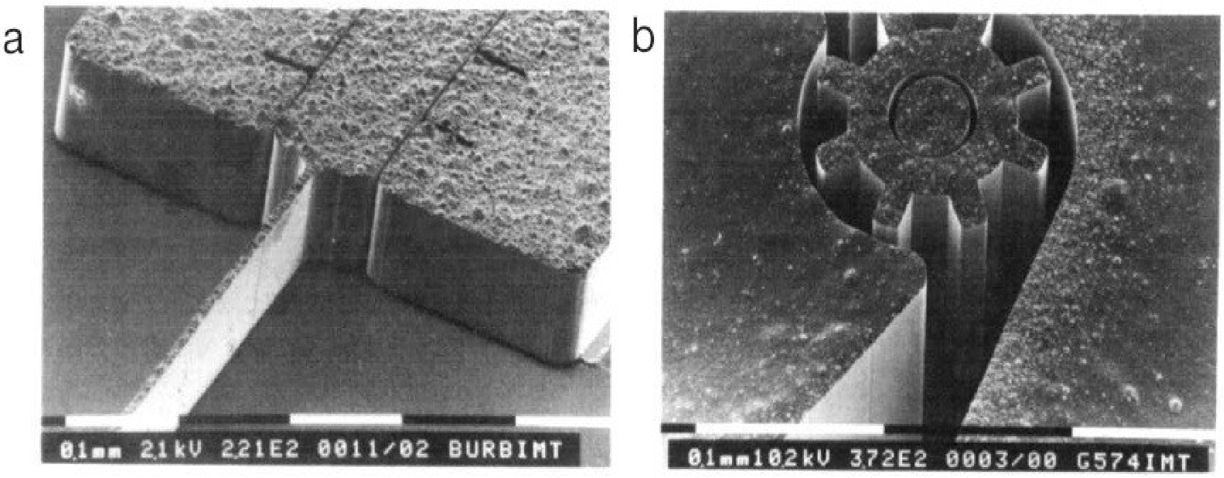

Figure 1.1: *(a) Detail of an acceleration sensor* [6] *and (b) microgear made from Nickel (gear dia. = 130 μm, height = 150 μm)* [6].

The LIGA technique takes place in steps, namely exposure, development, electroplating and forming. A thin X-ray absorbing resist layer is placed on a substrate, which is then exposed to synchrotron X-ray radiation. This transfers a pattern from a membrane to the substrate. The polymer resist layer of the mask, which is destroyed by X-rays, is dissolved to produce a template. A metal is then deposited in the empty spaces of the template up to the height of the resist or more by electrodeposition. After this, the unexposed layer of the resist is removed. The metal pattern constitutes of an insertion frame that is filled by an injection molding process [6]. A micrograph of components formed by LIGA is shown in Fig 1.1.

Such nc Nickel components and films have a very low amount of material and any corrosion attack can result in failure. Hence, it is of great interest to study the corrosion behavior and effects of HE on nc Nickel to gain an understanding and some degree of predictability. The subjects of this study are nc Nickel films, formed by electroplating and Physical Vapor Deposition (PVD) on a Silicon substrate.

Nickel is affected by both localized intergranular corrosion and HE. Applications of Nickel plating include aerospace components, chemical manufacturing equipment, oil and gas components, MEMS components and electronic chips [7]. These components remain susceptible to wear and corrosion of plated Nickel.

CHAPTER 2

OBJECTIVE

Corrosion and HE are issues of great concern in critical applications like microelectronics, aerospace and oil and gas components. Especially in the case of microelectronics, as the amount of material is very low, even a small corrosion attack or embrittled area can cause failure.

Nickel is susceptible to localized intergranular corrosion, so having a higher volume fraction of grain boundaries might increase the amount of corrosion. However, the large amount of grain boundaries over the surface of plated nc Nickel might distribute corrosion and make the attack more uniform and less in severity.

Grain boundaries also happen to be sites of hydrogen adsorption and promote its accelerated diffusion through the material structure. However, a predictive understanding of precise interactions has proven to be elusive. This is because the information on the configuration of boundary atoms is incomplete. Also, grain boundaries tend to have non-metallic species that introduce further complications. In any case, it can be assumed that increase in amount of grain boundaries will increase the hydrogen ingress and can embrittle nc Nickel.

The aim of this study is to understand the corrosion behavior of nc Ni and the fracture mode in the material as a result of the hydrogen embrittlement. Corrosion of the material shall be studied in aqueous environments of 3.5% NaCl and 0.1 N H_2SO_4. Hydrogen embrittlement of the same will be examined via microindentation after cathodically charging hydrogen.

CHAPTER 3

LITERATURE REVIEW

3.1 Nickel

Nickel is a metallic element of the transition series in the periodic table. It has a Face Centered Cubic (FCC) structure, ferromagnetic nature (at room temperature), a high melting point of 2647^{o} F (1453^{o} C). It is ductile, malleable and forms alloys readily as solvent and solute. Apart from that, it also resists corrosion by forming a passive oxide layer on its surface. This makes it susceptible to localized corrosion at defect sites [8].

The attractive properties of Nickel make it suitable for many applications. Its high strength, wear resistance and thermal stability is exploited by Nickel alloys and high strength steels alloyed with Nickel. These materials are used to make critical components like gas turbine blades, valves and chokes in the oil and gas industry, automotive turbochargers and exhaust systems, heat exchanger piping and cryogenic storage tanks. It is also an important component in memory-shape alloys and super elastic alloys. Such special alloys are used in medical devices and cellular phone antennae. Nickel-Titanium memory alloys are used in actuators, hydraulic connectors and spectacle frames [8].

Nickel is also a coating material in heavy engineering applications. Nickel coatings impart corrosion resistance (to moisture and alkalis), abrasion/erosion resistance and lubricity to coated material. A popular method of coating Nickel is electroless coating, which is conducted in the absence of an electric current. These electroless Nickel deposits contain small amounts of phosphorus, which increases the corrosion resistance and abrasion resistance of the coating. Nickel coatings are also lustrous, which gives the component a good appearance. These coating are very uniform in thickness and their mechanical properties like harness can be modified with heat treatments. Nickel coatings are also used in microchips for electronics and components in MEMS devices. Nickel acts as a barrier between magnetic media and the substrate in hard disks. It also protects the aluminum disc from corrosion. For MEMs applications, the LIGA technique is used to selectively coat complex and intricate geometries of Nickel onto a substrate.

The direct cost of corrosion is estimated at 276 billion, or ~3.1% of the nation’s GDP [9]. The largest use of Nickel and its alloys is in the area of corrosion. Two thirds of all Nickel produced is used to make stainless steel, where it promotes a ductile austenitic structure and corrosion resistance.

3.2 Nanostructured materials

Nanostructured materials are materials having a microstructure of a characteristic length less than the order of 100 nm. Their properties can be dramatically different from their bulk counterparts, having similar chemical composition but a microcrystalline (mc) structure. Ordinary bulk materials tend to have grain sizes larger than 1 micron. The difference in properties arises from the reduced dimension of nanometer sized crystallite and larger volume fraction of interfacial surfaces. As a result of their interesting properties, nanostructured materials have been the subject of extensive research since their introduction by Gleiter [10].

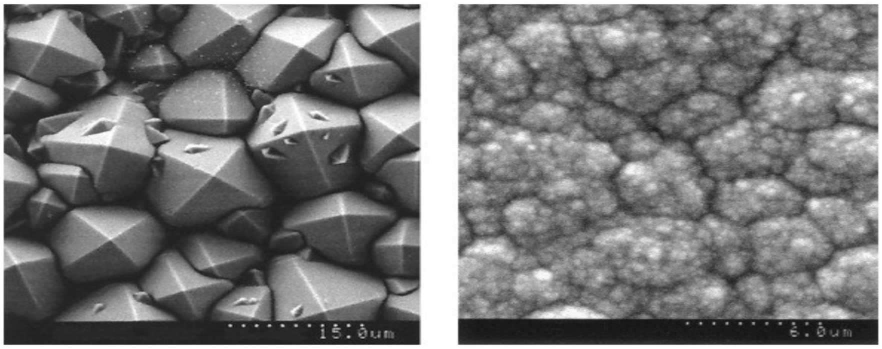

Figure 3.1: *SEM micrographs of typical microcrystalline (left) and nanocrystalline (right) Zn-Ni alloy* [11].

Due to the large amount of grain boundaries in nc materials, up to 49% of atoms can be boundary atoms [12]. This interfacial structure differentiates nc materials from their coarse grained counterparts. As the grain size in a nc material drops into the nanometer range, it develops interesting properties. These properties include improved structural/morphological properties (Fig. 2) [11], high strength/hardness [13], ductility that varies with strain rate, increased resistance to wear and potential for enhanced super-plastic deformation at lower temperatures [14]. These properties may not have been fully investigated, but there are sufficient studies that provide a general understanding of their potential benefits. There are studies that compare materials with grain sizes ranging from mc to nc materials. The remarkable improvement in mechanical properties of nc materials from mc materials can be seen in Table 3.1.

Table 3.1: *Mechanical properties of conventional and nanocrystalline Nickel* [1].

Property	Conventional Nickel [a]	Nanocrystalline Nickel	
		100 nm	10 nm
Yield Strength, MPa (25^{o} C)	103	690	>900
Yield Strength, MPa (350^{o} C)	-	620	-
Ultimate Tensile Strength, MPa (25^{o} C)	403	1100	>2000
Ultimate Tensile Strength, MPa (350^{o} C)	-	760	-
Tensile Elongation, % (25^{o} C)	50	>15	1
Elongation Bending, % (25^{o} C)	207	>40	-
Modulus of Elasticity, GPa (25^{o} C)	140	214	204
Vicker's Hardness, kg/mm^{2}	0.4	300	650
Work Hardening Coefficient	241	0.15	0
Fatigue Strength, MPa (10^{8} cycles/air/25^{o} C)	1330	275	-
Wear Rate (dry air, pin on disc), μm^{3}/ μm	0.9	-	7.9
Coefficient of Friction (dry air, pin on disc)		-	0.5

a: ASM Metals Handbook, ASM International, Metals Park, OH, Vol. 2 , p. 437 (1993)

The improved yield strength and hardness is predicted by the Hall-Petch relationship, shown in equation 1,

$$\sigma y = \sigma o + \frac{ky}{\sqrt{d}} \qquad Eq. 1$$

Here, σ_y is the yield stress, σ_o is the stress required for motion of dislocation, k_y is the strengthening coefficient and d is the grain size. According to the equation, the strength of the material increases with decreasing grain size.

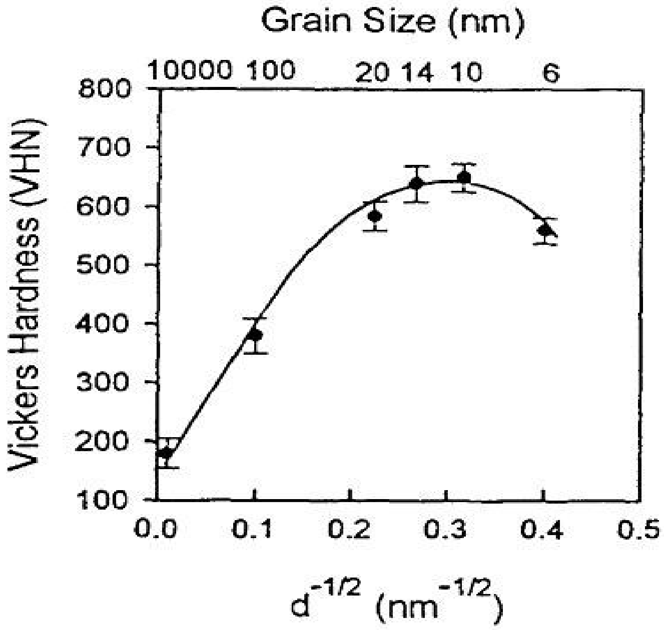

Figure 3.2: *Hardness of nanocrystalline Nickel as a function of grain size* [1].

Here, the pile-up of dislocations at grain boundaries is seen as the mechanistic process that resists plastic flow, with grain refinement. This trend is observed for most grain sizes, but as the grain size reduces below the order of 10 nm or so, the metal softens.

Fig. 3.2 gives the Hall-Petch and inverse Hall-Petch response. The underlying mechanism is not well understood, but it is hypothesized that dislocation sources cannot exist in a grain of such small size and the metals act more like amorphous materials. Meaning, dislocation pile-ups cannot exist to support the Hall-Petch relationship. Instead, an inverse Hall-Petch relationship is observed [14].

Mechanical properties of nc materials are seen to follow a predictable trend. However, this is not the case for all properties. Since there are different methods of synthesizing nc materials, the final structure of nc materials formed by, say consolidation of powders have a higher amount of porosity than electrodeposited structures. This has a marked effect on properties like Young's Modulus and Curie temperature [15].

3.3 Synthesis of nanostructured materials

Researchers have come up with a large number of synthesis methods for nanostructured materials. They can be sorted into five basic categories; solid state, liquid phase, vapor phase, chemical and electrochemical processing. Table 3.2 lists these categories, along with examples.

Table 3.2: *Basic categories of synthesis of nanostructured materials* [16].

Vapor Phase Processing	Liquid Phase Processing	Solid State Processing	Chemical Processing	Electrochemical Processing
• Inert gas condensation • Physical Vapor Deposition • Chemical Vapor Deposition	• Rapid solidification • Thermal spray coating • Solution precipitation	• Ball milling • Mechanical attrition • Crystallization from amorphous precursors	• Mixed alloy processing • Sol-gel processing	• Electrodeposition • Electroless plating

There are at least a few hundred variations of the above listed synthesis methods. However, this research is limited to the PVD technique.

3.3.1. Physical Vapor Deposition technique for synthesis of nanostructured materials

PVD is a vacuums deposition process that involves removal and deposition of material via purely physical processes like plasma bombardment or high temperature vacuum evaporation and condensation. There are various variants to this method, such as electron beam PVD, pulsed Laser deposition and sputter deposition.

Sputter deposition technique us used in this research. It may be defined as ejection of particles from a condensed solid target due to the impingement of energetic projectile particles. Since it was first reported in 1852 [17], the technique has evolved with periods of scientific attention and development in microanalysis and ultra-high vacuum technology. However, it is relatively recent that a sufficient understanding of the complex processes occurring on a solid surface during ion bombardment has been gained to develop reproducible and controllable use of the technique to grow a high quality of single crystals, complex alloys [18].

3.3.2.1 Mechanism

Most commonly, the sputter deposition technique involves energizing an inert gas like Argon with a DC power source in an ultra-high vacuum chamber, in order to form a glow discharge plasma. This is called DC-diode argon glow discharge (Fig. 3.7). Depending on the process, the base pressure in the chamber is kept between 10^{-6} to 10^{-8} Torr. The chamber is then back-filled to pressures between 10 to 100 mTorr with Argon. The chamber also contains a grounded substrate and a target with a negative potential mounted opposite to it. The target acts as the cathode and the substrate acts as an anode [19].

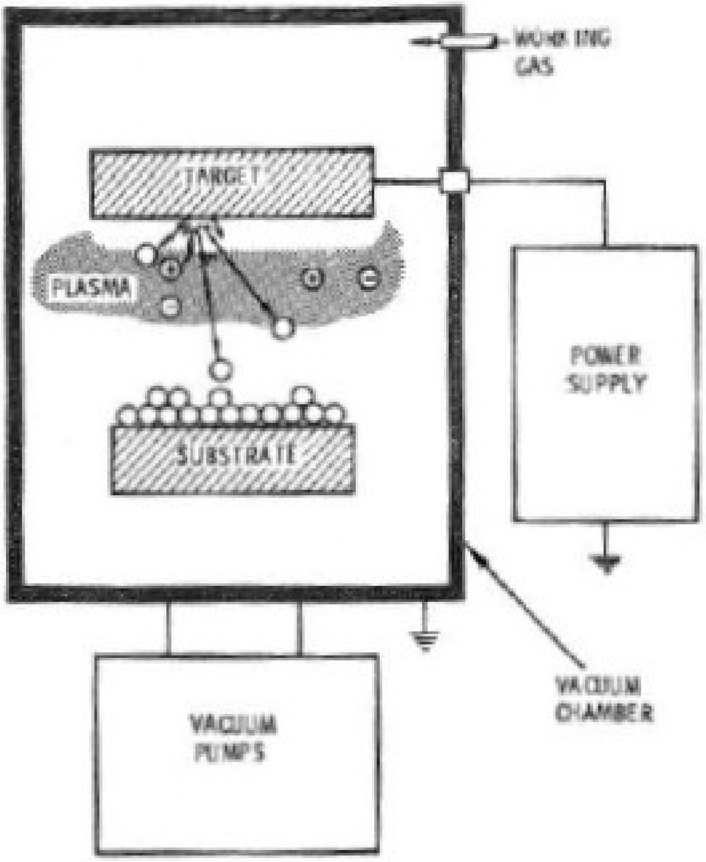

Figure 3.3: *Schematic diagram of a sputtering system assembly* [18].

When the DC power source is turned on, a negative potential is provided to the target. All free electrons will be accelerated away from the negatively charged cathode towards the inert gas. These free electrons will drive away the electrons from the gas atoms, leaving the gas positively charged. The negative charge on cathode initiates a positive gas ion bombardment. The bombardment on the target results in a physical ejection of target atoms, which end up on the surface of the substrate to make a layer of target material [18] [20].

However, the diode sputtering technique has two drawbacks. The free electrons also bombard the substrate, which can damage its structure and the deposition rate is slow. A recent development in the sputtering sources involves use of magnetic fields to confine the plasma, called magnetrons. The magnetrons trap the free electrons in the magnetic field and cause them to carve a circuitous path in a confined area below the target. As most electrons are found in this area, the plasma produced and confined as well [20]. These magnetrons are found from small ring forms to long rectangular planar magnetrons and cylindrical magnetron posts or hollow cathodes [18].

3.3.2.2 Factors affecting microstructure and properties

There are several factors that decide the properties and microstructure of a DC Magnetron Sputter deposited Nickel film, such as power applied, rate of deposition, argon gas flow rate, and temperature and so on.

The film deposition rate is defined as the ratio of film thickness to deposition time. Now, the kinetic theory of gases states that the mean free path of the gas species is inversely related to its pressure. Mean free path is the distance a particle travels before it collides with another gas molecule. Meaning, higher Argon pressures causes a high number of collision events between Nickel and argon atoms, which scatters some Nickel atoms away from the substrate. This translates to a lower deposition rate. This trend is observed in various literatures [21] [22]. Fig. 3.4 plots the deposition rate as a function of variables [23].

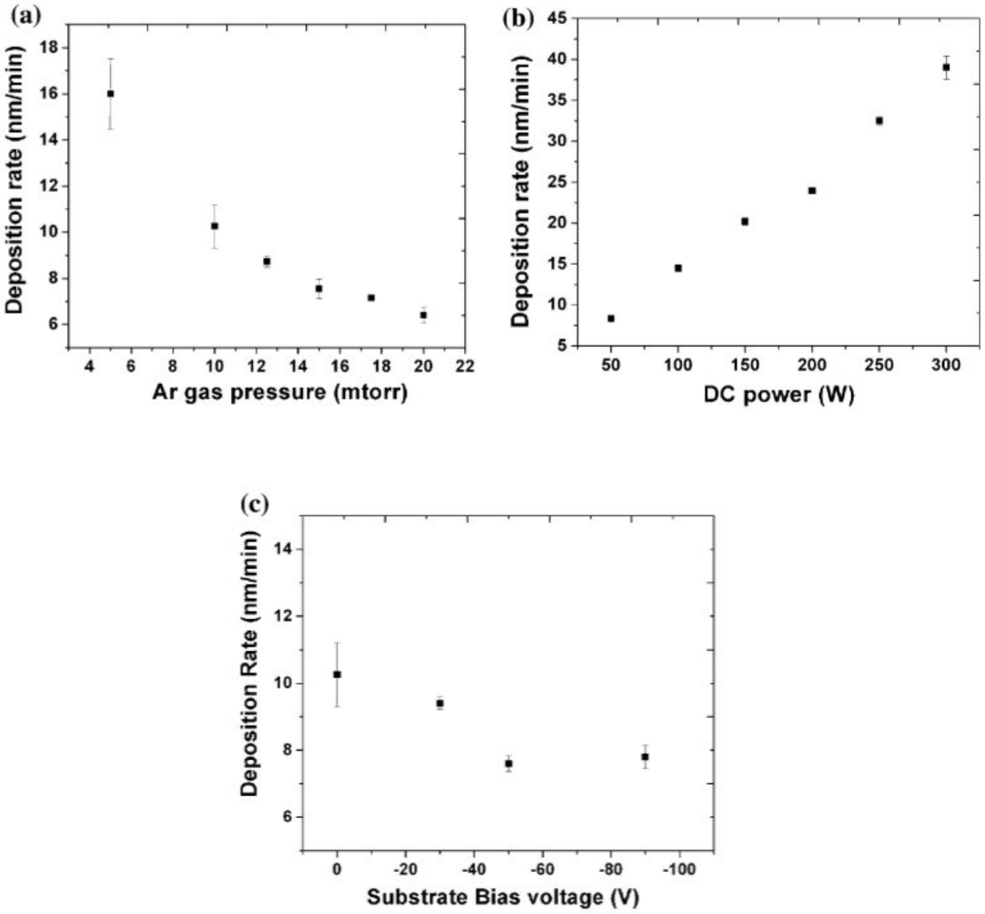

Figure 3.4: *Deposition rate as a function of (a) Argon gas pressure, (b) DC power and (c) substrate bias voltage, for Ni films deposited at room temperature* [23].

The argon ion flux and its average kinetic energy are functions of applied DC voltage. Thus, it seen that the deposition rate increases linearly with DC power (Fig. 3.4).

The variation in deposition rate with respect to substrate bias voltage, at a constant power of 100 W and Ar gas pressure of 10 mTorr, is shown in Fig. 3.4c. It can be seen from this graph that, on application of a small negative bias voltage to the substrate, positive Ar ions are attracted to the substrate. This results in some of the deposited film to sputter-off. Further increase in substrate bias would result in significant lowering of deposition rates.

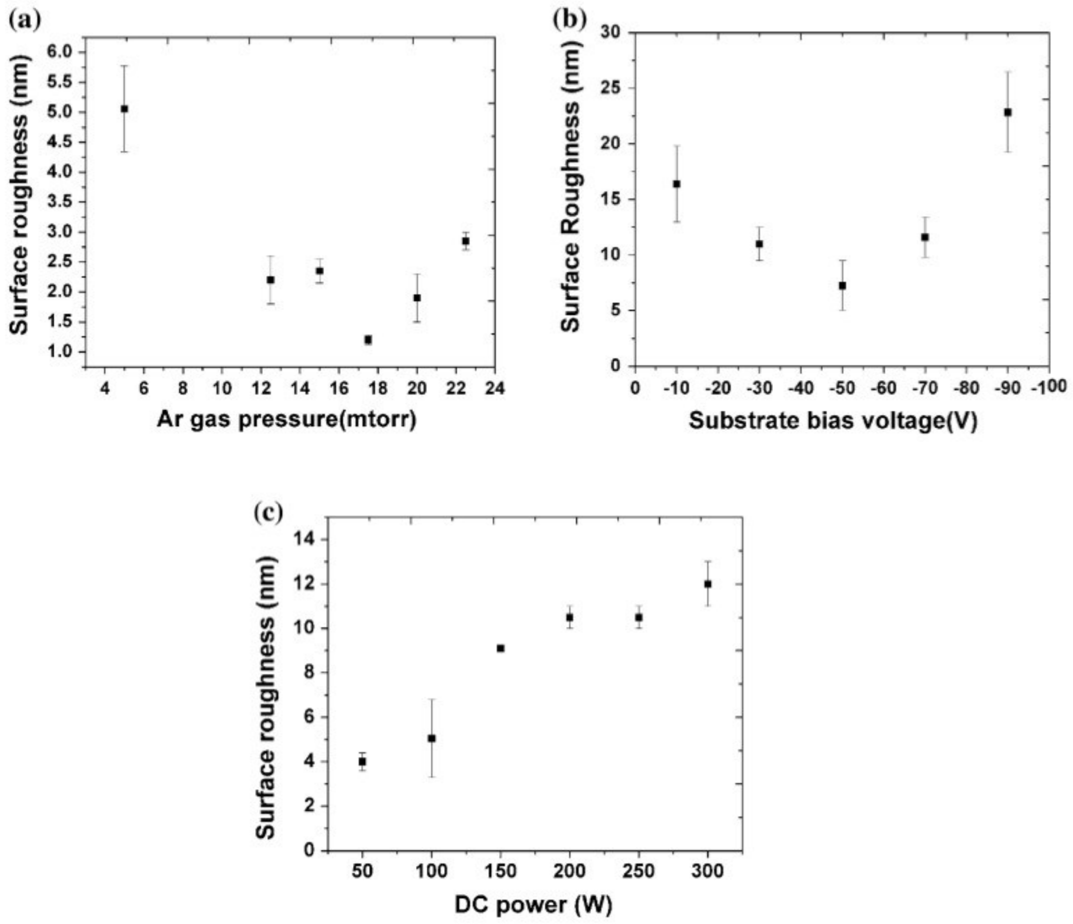

Figure 3.5: *Surface roughness as a function of (a) Argon gas pressure (b) substrate bias voltage (c) DC power, for Ni films deposited at room temperature* [23].

In addition, Gai et al. [24] observed that the re-sputtering of deposited Ni atoms due Ar species enhances the Ni mobility through momentum transfer leads to a dense film and formation of a nuclei island. Subsequent nuclei islands that formed overlap with the previous ones and the mean grain size also tends to increase.

A plot of variation in roughness of sputter-deposited Ni films on a Si substrate with varying Ar gas pressures is seen in Figure 3.5a. On increasing gas pressure, the surface roughness was seen to decrease. Due to the collision events of Ni adatoms with Ar gas species, the average kinetic energy of Ni adatoms decreases and results in a broader distribution along the surface of the substrate. This decreased mobility and high nucleation density is responsible for fine grains with a smooth surface. However, any increase in pressures beyond 17.5 mTorr caused a rise in the surface roughness. It was seen that this rise in gas pressures contributes to a preferred texture structure of (200) plane and (100) orientation in the Ni film [23].

Films deposited at relatively low Ar gas pressure, room temperature and no substrate bias [24] possess a (111) texture, along with the presence of (200) and (220) as well. Increasing the substrate bias produces a stronger (111) texture, along with improved crystallinity [25]. Thickness of films deposited played a negligible role, as the trend was observed in various thicknesses [23].

According to Figure 3.5b, surface roughness declines on increasing substrate bias. Up to a bias of -50 V, Priyadarshani et al. [23] observed a smooth film, as the bias helped surface migration of ions to fill the voids created during film growth. However, film roughness increased beyond a bias of -50 V. This was explained by the enhanced ion bombardment on a growing film, which may cause re-sputtering of already deposited material from the substrate.

DC power supply has a limited effect on film roughness. Figure 3.5c demonstrates how an increase of power from 50 W to 300 W changes the roughness by only 8 nm. DC power contributes to the number density and mobility of adatoms. When applied DC power is high, the condensation of adatoms suffers due to their high mobility. This reduces the ability of adatoms to fill void boundaries and contributes to surface roughness [23].

3.3.2.3 Advantages of Sputtering

Some advantages of the DC Magnetron Sputtered films are listed below [19]:

- Improved coating adhesion, due to the ability to “sputter-clean” and pre-heat substrate
- Uniform coating thickness by virtue of gas scattering effects and the ability to rotate and displace substrate with respect to vapor source.
- Control over coating structure and deposition rate by varying deposition parameters

- Multilayer deposition and alloy deposition of complex materials possible
- Highly pure deposits through use of vacuum
- Low deposition temperatures
- No post coating treatments needed

3.4 Corrosion

Corrosion is an irreversible interfacial reaction of a material with its environment, resulting in the loss of material or in the dissolving of one of the constituents of the environment into the material. It also includes material damage due to the absorption of a constituent of the environment, such as hydrogen absorption into steel, which causes embrittlement and thus impairs the mechanical properties of the material [26]. Such reactions deteriorate the material. Pure metal is extracted through metallurgical processes from their oxide-based ores. Corrosion revert metals back to their oxide form. Most corrosion phenomena occur through electrochemical reactions caused by a potential difference between an anode and a cathode. The anodic metal gets converted from a metallic to an ionic form, through oxidation. Hence it is important to understand these electrochemical reactions in order to understand the nature of corrosion.

Most metals tend to corrode when in contact with water (or moisture), salts, acids, bases, oils and reactive solids. In these conditions, the metal may corrode uniformly. However, some metals, like Nickel, are resistant to corrosion. They form a layer of oxide on the surface which passivizes the component from corrosion. However, they are susceptible to localized corrosion at interruptions in the passive layer, such as a scratch or a defect. The defect site will act as an anode to a very large cathodic area and corrosion will occur. This very localized type of corrosion forms pits or holes in the metallic component and penetrates the entire component. Such type of corrosion is called pitting corrosion. Sometimes, corrosion will be aided by physical forces of wear, abrasion or erosion that can continually remove passive layer of the metal, increasing the rate of corrosion. Furthermore, heterogeneity in a material, such as grain boundaries, creates a potential difference which causes Intergranular corrosion. More examples of localized corrosion cells are given in Table 3.3.

Fig. 3.6 represents the corrosion behavior of an anodic material with an Evans diagram. This diagram plots the logarithm of the absolute value of the current as a function of the potential and indicates the possible variations of the anodic behavior of various metals in aqueous solutions.

Table 3.3: *Origin of corrosion cells* [26].

Origin of potential difference	Designation
Contact between two different metals	Galvanic corrosion
Difference in oxygen accessibility	Differential aeration cell, Crevice corrosion
Grain boundary precipitation	Intergranular corrosion
Local depassivation by aggressive anions	Pitting corrosion
Difference in temperature	Corrosion due to thermal cells

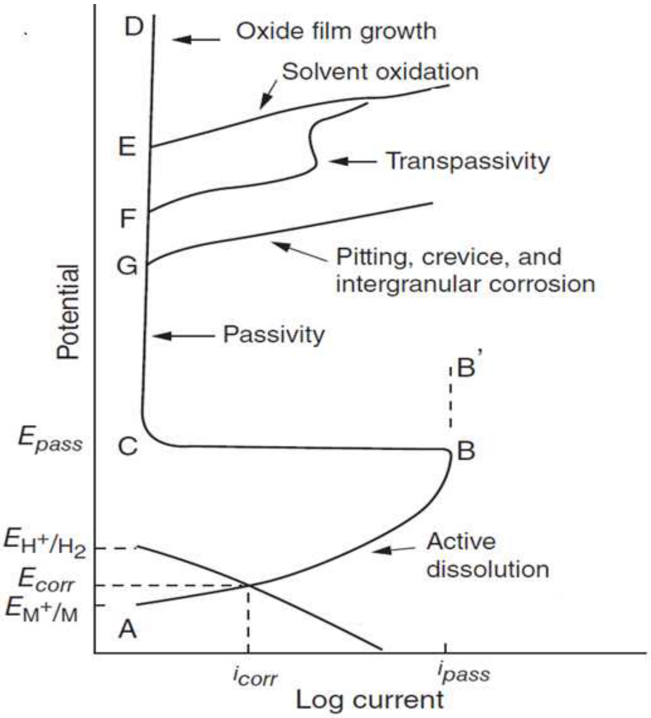

Figure 3.6: *Variation of anodic behavior of passivation metals in aqueous solutions* [27].

As the potential increases in the positive direction from E_{corr} to B, anodic dissolution of metal occurs. For passivating metals, a threshold is reached, where the oxide film is formed. The logarithmic value of current increases linearly, with the potential to the threshold. After this threshold, a constant current is reached. However, the log current can vary by a few orders of magnitude in the range of B to C during the passivation. This potential is called passivating potential E_p and corresponding current is called passivating current i_p. On further raising the potential, the current remains the same and the oxide layer grows thicker. For nonconductive passive films, a very high potential up to D can be reached.

On the other hand, if the passive film consists of cations that can be oxidized to a higher oxidation state and form soluble products, the current may increase at a lower anodic potential (F). This indicates transpassivity of a metal and is accompanied with further dissolution of metal. The passive films formed by Nickel are conductive. Hence, when a high enough potential (E) is reached, the current will rise significantly. In aqueous systems, this corresponds to oxidation of water and generation of oxygen. In other words, passive metals and alloys have a critical potential at which the passive film becomes unstable, leading to localized corrosion (G). This point is reached particularly in halide and chloride solutions.

A Pourbaix diagram can be used to take into account the various oxides of a metal and the conditions in which they form. A Pourbaix diagram is a graphical representation of the reversible potential, as a function of pH. The diagram indicates the equilibrium conditions of the chemical products of reaction/s, assuming all the reaction/s have taken place.

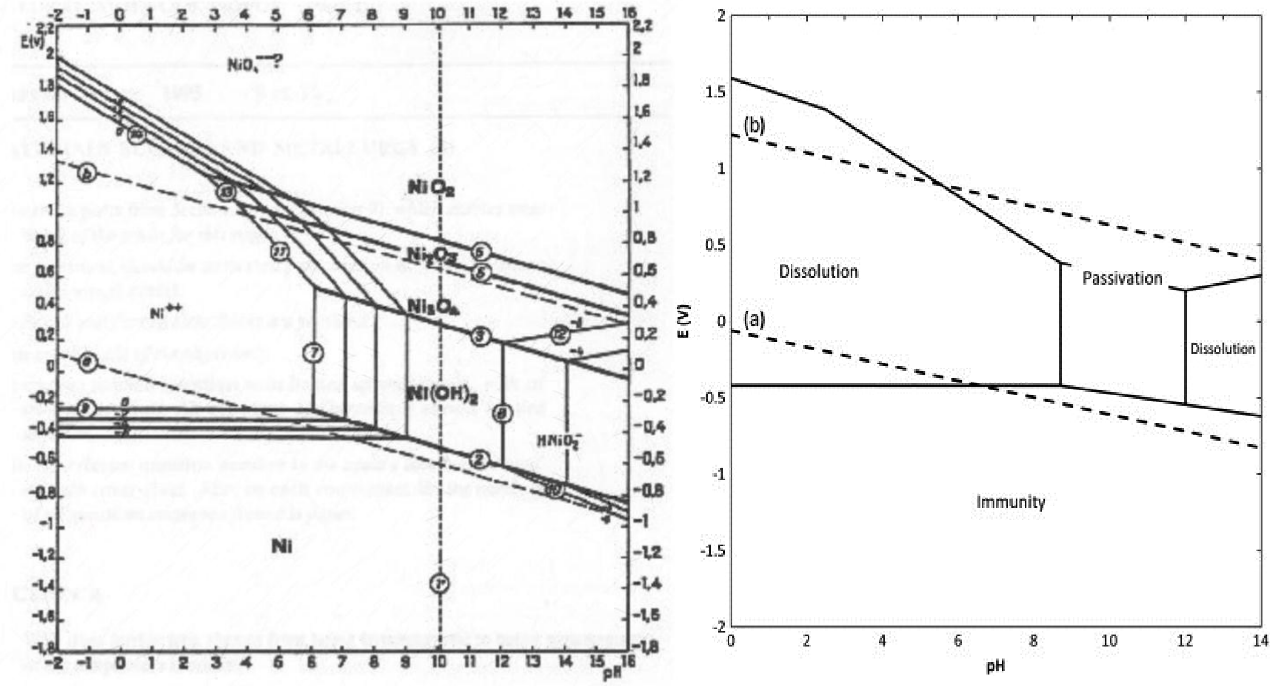

Figure 3.7: *Pourbaix diagram for Ni showing soluble ions (left) and corresponding corrosion regime changes (right)* [28] [29].

Corrosion is possible in the areas of the diagram where soluble ions of the metal are stable. This allows us to create conditions to avoid corrosion, by changing the pH and potential. However, the thermodynamics of the reactions and products shown by the diagram do not indicate the rate of these reactions. In the Pourbaix diagram for Ni (Fig. 3.7), the conditions where soluble ions are stable, corrosion (dissolution) takes place and this region is termed as active. The passive region indicates conditions where Ni forms a passive film. And in the immunity region, Ni is does not corrode.

3.4.1. Corrosion of nanocrystalline Nickel

Nickel metal, its alloys and composites have been fabricated in mc and nc form. Their corrosion behavior has also been explored by some researchers, for different systems. For example; Wang et al. [30] investigated the electrochemical and corrosion behavior of nc Nickel when affected by corrosive environment (10% NaOH solution). On reducing the grain size from 3 μm to 16 nm, they found the corrosion resistance to increase. They attributed this to a faster formation and good integrity of continuous Nickel hydroxide passive film. Qin et al. obtained similar results when they exposed nc Nickel (2 μm to 16 nm grain size) to 10% NaOH and 3% NaCl solutions. NaCl solution is a typical environment to evaluate the corrosion resistance of a material. Fig. 3.8 shows an example of polarization curves of nc Nickel of different grain sizes in 3 % NaCl [31]. A negative shift in potential is seen with decreasing grain size, but there is also a significant reduction in current density when grain size reduces from 2μm to 16nm. Similar results are also seen in 10 % NaOH solution. These tests indicate that nc Nickel films have multiple nucleation sites for passive films and show better corrosion resistance [31].

Studies by Rofagha et al. [32] concluded that under potentiostatic conditions in a 2 M H_2SO_4 solution, with SCE reference electrode at 1.2 V, nc Nickel corroded uniformly after exposure of 2000 seconds. On the contrary, pitting corrosion was seen on conventional (mc) Nickel. The passive layers for both nc and mc Nickel were nearly equal in the study, but the nc Nickel passive film had more defects. The allowed a more uniform breakdown of the film in nc Nickel. In contrast, the passive film breakdown in mc Nickel occurred at the grain boundaries and triple junctions. The nc films also displayed a passive current density that was 1 order of magnitude higher than conventional Nickel. A positive shift of -200 mV (Fig. 3.9) was observed in the corrosion potential, which was explained as a result of catalysis of hydrogen evolution reaction. It can be seen that, at higher potential, passivation does not occur. This is due to the oxidation of the passive film to a higher valence, as predicted by the Pourbaix diagram.

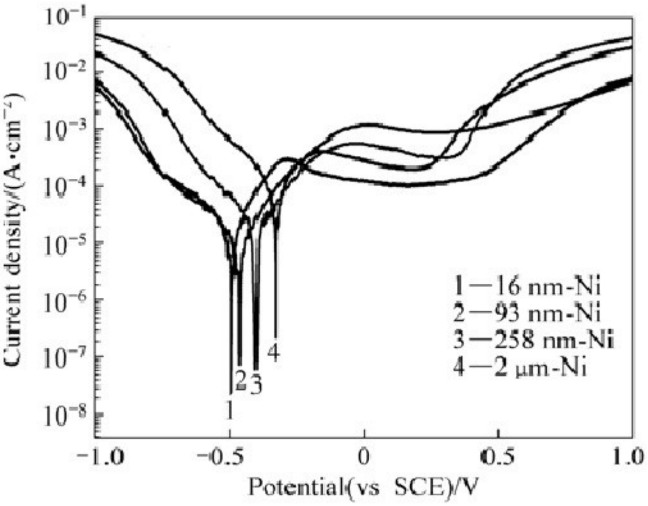

Solution	Sample	Corrosion potential (vs SCE)/V	Corrosion current density/($\mu A \cdot cm^{-2}$)
3%NaCl	16 nm-Ni	−0.494	5.21
	93 nm-Ni	−0.462	7.55
	258 nm-Ni	−0.401	15.89
	2 μm-Ni	−0.325	53.43

Figure 3.8: *Polarization curves for Nickel films of different grain size in 3 % wt. NaCl* [31].

Similarly, Mishra and Balasubramanian [33] tested the corrosion and electrochemical properties of nc Nickel, varying from 8 to 28 nm in grain size, when exposed to 1 M H_2SO_4. Their observations concur with those of Rofagha et al. The corrosion rate of exposed nc Nickel was slower than its bulk counterpart. Nanocrystalline Nickel was also found to have a higher passive current density and higher break down potential than mc Nickel, because of the large number of defects in the nc passive film.

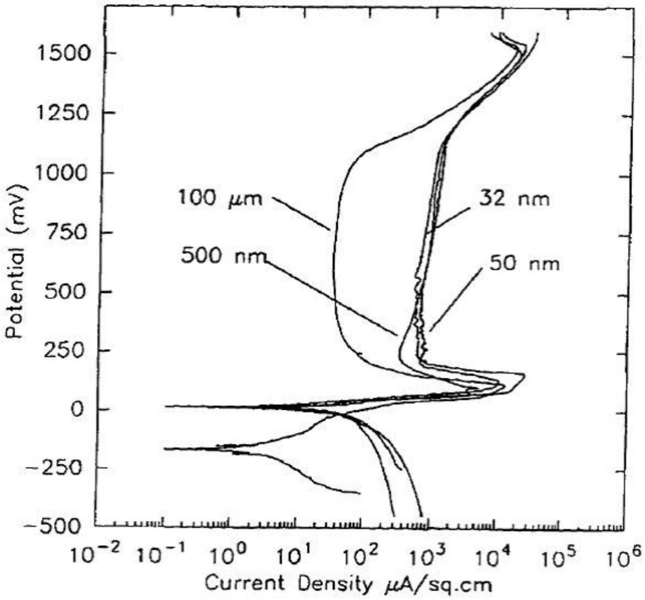

Figure 3.9: *Polarization curves of Nickel films of different grain size in 2 M* H_2SO_4 [32].

The above investigations pertain to electrodeposited nc Nickel films. Although more research needs to be done to evaluate corrosion properties of sputtered Nickel films, improved corrosion resistance is noted in Nickel films deposited by PVD technique as well [34]. In summation, nc Nickel deposits display an active-passive-transpassive behavior, similar to mc Nickel. The differences are evident from the open circuit potential and passive current density.

3.5 Hydrogen Embrittlement

Hydrogen reduces the service life of many metallic components. Such reductions may be manifested as blisters, enhanced creep, decrease in fatigue resistance and most commonly, unexpected macroscopic brittle fracture. The ASM handbook lists five specific types of hydrogen induced damage to metals and alloys, namely

- Hydrogen embrittlement
- Hydrogen induced blistering
- Cracking from precipitation of internal hydrogen

- Hydrogen attack
- Cracking from hydride formation

An unexpected macroscopic brittle fracture is often termed as hydrogen embrittlement [4]. Sometimes, mechanical forces may work synergistically with hydrogen embrittlement to induce Stress Corrosion Cracking (SCC). This research focuses on hydrogen attacks that do not involve a phase transformation in materials. It is generally accepted that hydrogen dissociates to get absorbed on a material surface or crack tip, and then recombines in the microstructure of the material. Thus, the presence of atomic hydrogen is required on the surface of metal for it to be absorbed. Fig. 3.10 schematically illustrates this process.

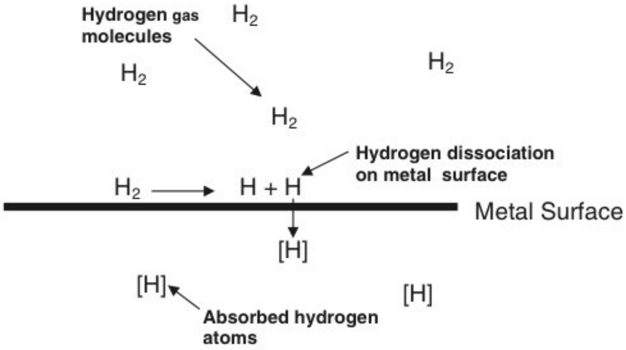

Figure 3.10: *Hydrogen absorption in metals exposed to a gaseous hydrogen environment* [4].

The condition of the metal surface decides the efficiency of the disassociation process on the metal surface. For example, exposure to acidic solutions like hydrogen sulfide corrodes the metal and introduces hydrogen into its surface at a much higher rate, than exposure to hydrogen gas. And presence of passive films hinders the absorption of hydrogen. Once absorbed, the hydrogen in the metal can be present in interstitial sites in the lattice or in crystalline defects, such as grain boundaries, vacancies, dislocations or cracks [4].

Although the problem of hydrogen embrittlement has existed for a long time, a conclusive and universal understanding of the phenomena and its mechanism at the microscopic scale are still under debate. However, the various processes leading up to the debatable interactions in question are schematically illustrated in Fig. 3.11.

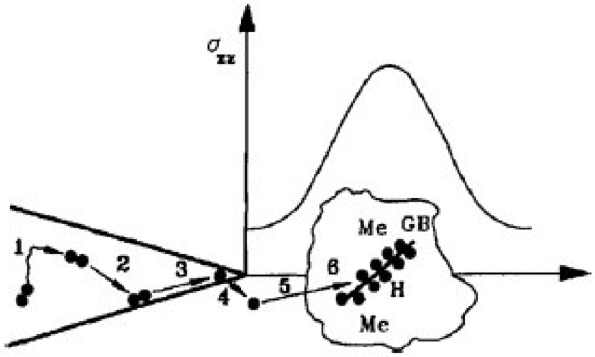

Figure 3.11: *Rate controlling steps for the transport of hydrogen to the fracture propagation zone* [35]*. 1. Transport of the gas to the crack tip, 2. Physical adsorption, 3. Dissociative chemical adsorption, 4. Hydrogen entry, 5. Diffusion of hydrogen in the crack tip, 6. Hydrogen-dislocation interaction.*

The complicated interactions, mentioned last on the list, between different aspects of HE have resulted in a large number of studies, with sometimes controversial findings. Numerous systems and circumstances in terms of environmental, mechanical and intrinsically material aspects have contributed to this situation. For these reasons, Barnoush [5] holds the assumption that HE may be governed by multiple dominant mechanisms. The two mechanisms considered in majority of the literature are HEDE and HELP.

3.5.1. Hydrogen Enhanced Decohesion

The HEDE mechanism suggests that hydrogen lowers the host metals' atomic cohesion by segregating at critical points like grain boundaries and induces (or aids in inducing) intergranular fracture, after a finite amount of plastic strain [36].

The nature of hydrogen dictates its attraction to expanded lattices, defects and dislocations. Grain boundaries have a large concentration of defects and are a prime example of such a region in a metal's microstructure. Cracks have a tendency to progress in the direction of least resistance. With a higher concentration of defects, grain boundaries serve as a preferential direction for crack growth and have a lower crack growth threshold (K_{TH}). For a pre-existing crack or micro-crack, hydrogen atoms are further supplied to the crack tip from adjacent parts of the fracture via surface diffusion. Effects of hydrogen have been studied thoroughly for various Nickel and steel microstructures.

One such study conducted by Kampe and Koss [37] revealed intergranular fracture at grain boundaries, for pure polycrystalline Nickel undergoing multi-axial deformation. Fractography of the samples show a loss of ductility due to hydrogen. This was initially manifested as isolated micro-cracks; and increased exposure to hydrogen lead to an increase in density of micro-cracks. Soon, a critical point was reached where the micro-cracks linked up to cause failure. McMahon [38] observed similar intergranular cracking in steel due to interface decohesion. The overall fracture was attributed to dissolved hydrogen in crystal lattice and embrittling impurities segregated at grain boundaries. These studies indicate loss in ductility and decohesion of grains at grain boundaries during fracture.

3.5.2. Hydrogen Enhanced Localized Plasticity

The HEDE mechanism deduces that the presence of H atoms lowers the surface energy of grain boundaries and decreases the cohesion between host atoms at critical regions of the microstructure. There have been several experimental studies that support this mechanism. However, in those experiments, the brittleness and plasticity coexist. The presence of stress does not allow a direct quantification of the effect of hydrogen in embrittling the material.

According to the HELP mechanism, the presence of hydrogen locally decreases the stress required for plastic deformation and causes failure of materials by plastic rupture. It suggests that hydrogen reduces the barriers to dislocation motion and shear localization occurs due to preferential diffusion of hydrogen in critical regions. This gives rise to enhanced plasticity, as regions with high hydrogen concentration tend to have lower flow stresses. Robertson and Birnbaum [39] observed that the presence of hydrogen significantly decreased the stress required to induce plastic deformation, in an HVEM study. Also, a stress concentration at the tip of crack promoted localized hydrogen diffusion in front of the crack tip. It was observed that at a constant stress, presence of hydrogen propagated the crack. In its absence, the crack ceased to propagate. Researchers in favor of the HELP mechanism suggest that strain hardening of materials during testing might mask the increased ductility caused by hydrogen [40].

Both proposed mechanisms have their merits and demerits. However, to determine the hydrogen failure mechanism for a particular system, a more comprehensive study is required to fully understand the hydrogen-metal/defect interactions and the role of hydrogen concentration gradient, fugacity and material surface conditions on these interactions.

3.5.3. Hydrogen Embrittlement in nanocrystalline Nickel

The permeation of hydrogen through Nickel microstructure has been studied for Nickel with varying grain sizes. Oudriss et al. [41] investigated the specific role of grain boundaries on the diffusion of hydrogen. They exposed electodeposited and annealed Ni to 0.1 N NaOH under cathodic polarization with current density of 20 mA/cm^2. The diffusion curve for hydrogen permeation reveals that the small grained Nickel had the highest computed hydrogen diffusivity coefficient. This study corroborated the results of Brass and Chanfreau [42], who prepared and charged Nickel samples by the same method.

Oudriss et al. assumed that intrinsic dislocations in grain boundaries only accommodate the grain misorientations, causing geometrically necessary dislocations (GNDs). Their study correlated irreversible hydrogen trapping sites to these GNDs, which increase with decreasing grain size.

Data presented in Fig. 3.12 compares hydrogen diffusion coefficient to grain size of Nickel. The first domain shows an increase in diffusion coefficient until a critical grain size is reached. In the second domain, the diffusion coefficient decreases with grain size. This decrease is attributed to the increase in hydrogen trapping sites found in GNDs. In the third domain, a rise in the diffusion coefficient is noted [41].

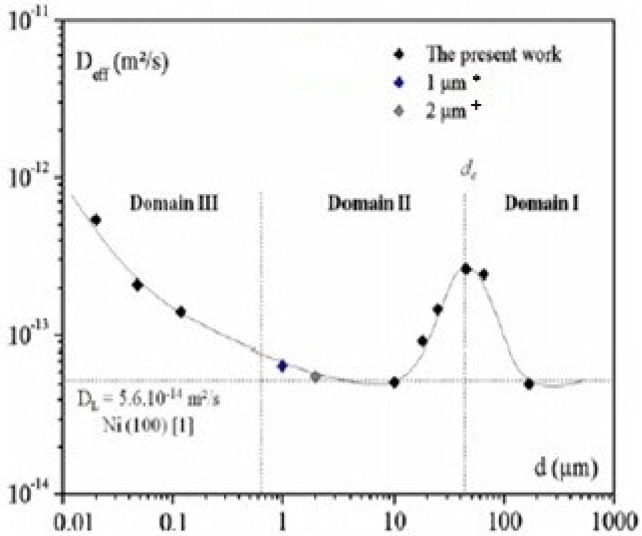

Figure 3.12: *Influence of grain size on diffusion of hydrogen in polycrystalline Ni* [41], *[43], +[44].

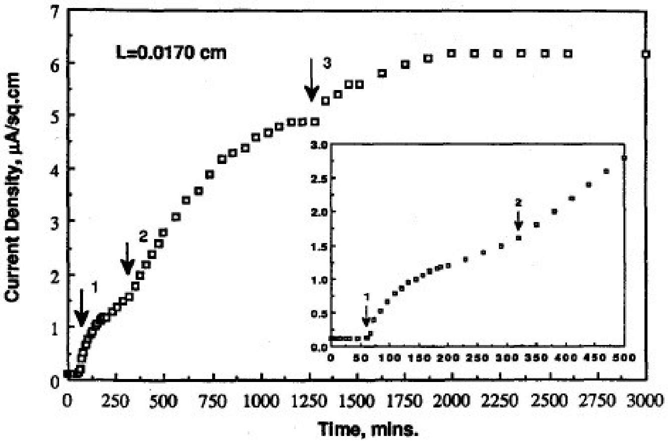

Figure 3.13: *Anodic exit current as a function of cathodic charge time (t) at 0.1 mA/cm^2 for a nanocrystalline Ni foil of thickness L* [45].

This is explained by the increase of short-circuit diffusion due to increased triple junctions in nc materials, initially suggested by Palumbo et al [45]. They exposed nc Nickel (grain size ~ 17 nm) to hydrogen via electro-permeation method (0.1 N NaOH solution), which links hydrogen adsorption to current density of the Nickel. Three distinct breakthrough current densities we observed, indicating separate diffusion paths of grain boundaries, triple junction and lattice itself (Fig. 3.13). This indicates that hydrogen diffusion is accelerated in vicinity of grain boundaries and triple junctions. Since nc materials have a higher density of such sites, they are expected to be more vulnerable to hydrogen embrittlement as compared to its microcrystalline counterparts.

CHAPTER 4

EXPRIMENTAL

4.1 Materials

4.1.1 Substrate

Silicon (100) wafers were used as substrate for this research. A chromium adhesion layer was sputter deposited on to the Silicon substrates. The Cr layer was used to improve the adhesion of Nickel to the Si substrate.

4.1.2 Thin film Nickel

To evaluate the properties of nc Ni in a corrosive and hydrogen environment, a number of samples were prepared on Si (100) substrate. Deposition of nc Ni was performed by DC magnetron sputtering.

The sputtering system used was assembled in-house in the SaNEL Laboratory. It is equipped with three sputtering guns, two DC and one RF power sources and a water cooling system that limits the usable power to 1000 W. The substrate holder can be rotated and heated to 900 ^{o}C. The chamber is evacuated to the order of 10^{-7} Torr with a rough pump, followed by cryogenic cooling pump. Multiple gas lines are connected to mass flow controllers and a control box to regulate the flow of gasses into the chamber and control the pressure of the system.

Multiple Nickel samples were prepared to determine optimal coating parameters using the magnetron sputtering system. The sputter deposition of the samples was conducted as per Table 4.1.

Figure 4.1: *Physical Vapor Deposition system at SaNEL laboratory, UTA.*

Table 4.1: *DC magnetron sputtering conditions.*

	Deposition material	Power (W)	Working pressure (mTorr)	Ar Gas flow rate (sccm)	Substrate Bias (V)	Thickness (nm)	Time (min)
1	Cr	200	20	20	-	-	10
	Ni	150	10	20	-	650	90
2*	Cr	200	20	20	-	-	10
	Ni	100	10	20	-200	1400	60

*Deposition #2 was conducted with a new target, which resulted in a thicker coating, despite application of a substrate bias.

4.1.2 Bulk Nickel

A solid wrought Ni 200 rod (diameter = 2.54 cm.) was machined to extract a reference. The 0.5 cm. thick section was mounted on an Aluminum stub (with silver paste) in epoxy. A threaded hole was tapped through the epoxy into the Aluminum stub to make electrical contact for electrochemical tests. The 5.06 cm^2 area of exposed Nickel was mechanically polished to 600 grit and rinsed with de ionized water and Methanol.

4.2 Material Characterization

4.2.1 X-Ray Diffraction

X-ray diffraction (XRD) was performed on a Siemens Krystaloflex 810 D500 machine. The X-ray diffraction was performed by low glancing angle diffraction technique. Here, the detector moved from a 2θ angle of 40^o to 80^o and the Cu K_α X-ray source remained at 10^o (wavelength = 1.542 Å). The peak broadening and Full Width Half Maxima (FWHM) from the diffraction results was used to calculate the grain size (d) from Scherrer's formula.

$$d = \frac{0.94 * \lambda}{0.5B * Cos\theta} \qquad Eq\ 2$$

Here, θ is half of the reported peak's centroid in radians, λ is the wavelength of X-ray source, B is the FWHM in radians and d is the crystal or grain size of tested sample.

4.2.2 Surface morphology

The surface morphology, coating thickness and depth profile of corrosion pits were studied using a Veeco Wyko NT9100 optical profilometer. This instrument employs coherence scanning interferometry to generate three dimensional surface maps of samples under examination.

An Agilent 5500 Scanning Probe Microscope (SPM) was also used as an AFM, in non-contact or tapping mode, to analyze the topography of nc Nickel coatings.

4.2.3 Scanning Electron Microscopy (SEM) and Energy Dispersive Spectroscopy (EDS)

A Hitachi S-3000N variable pressure SEM was used in conjunction with an EDS attachment was used at an acceleration voltage of 20 kV and working distance between 12 and 20 mm to analyze the surface and chemistry of samples at different magnifications. A Hitachi S-5000H SEM was also used to study samples at a higher magnification. Both bulk and nc Nickel samples were analyzed before and after various tests.

4.2.4 Electrochemical tests

A standard K0047 Corrosion cell by Princeton Applied Research was used along with a Princeton Advanced Research Potentiostat Model 273A, connected to a computer. 352 Corware III software interface controlled the potentiostat. All experiments were carried out with 3.5% NaCl or 0.1 N H_2SO_4 electrolyte prepared with de ionized water. Potentials were measured against Saturated Calomel Electrode (SCE).

Bulk Nickel was mounted and connected with a stainless steel rod that was threaded into the mounting, as explained earlier. A thin gold coated copper wire was placed on the nc Nickel coating and secured with electroplating tape. The thin wire was then encased in a glass tube with a Teflon cap that had a small opening for the wire. Microstop lacquer was used to seal the tube.

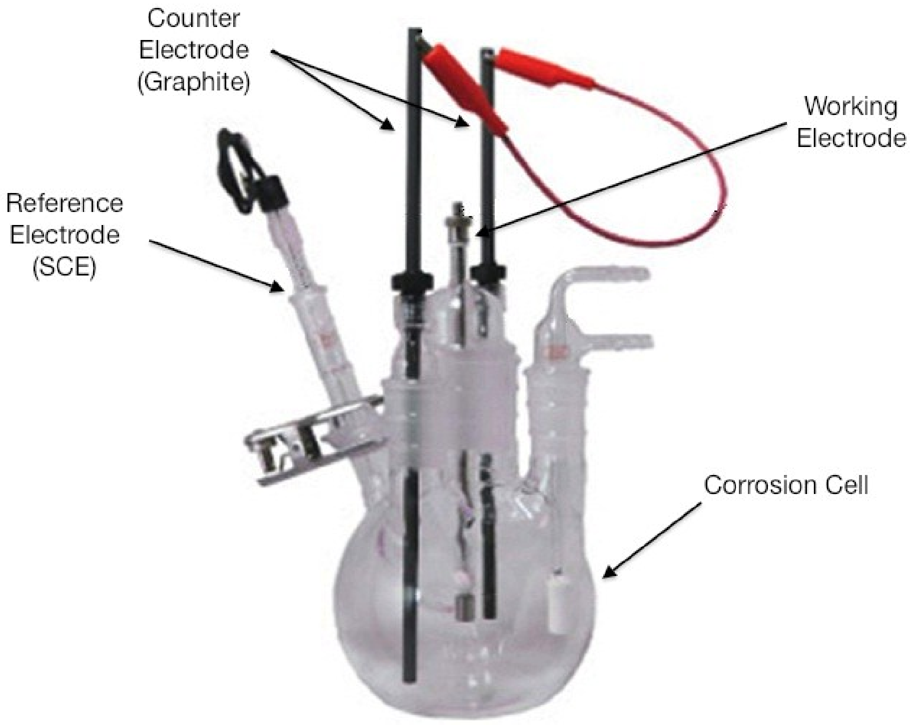

Figure 4.2: *The K0047 Corrosion cell set up.*

4.2.5.1 Corrosion Potential vs. Time measurement

This test is done without external input of power to obtain a steady state potential, at which corrosion reactions can be assumed to occur at equilibrium. This stable potential is called Open Circuit Potential (E_{ocp}). The time taken to reach this equilibrium depends on the system. This test was carried out in aerated conditions till the potential stabilized.

4.2.5.2 Anodic Polarization Testing

These tests were carried out in both 3.5% NaCl and 0.1 N H_2SO_4 solutions in de aerated conditions. The system was purged with Argon gas 20 minutes before the starting the experiment. The purging was carried out through the experiment as well to achieve de aeration. The anodic polarization was carried out in the range of 200 mV below E_{ocp} to 800 mV above E_{ocp} at a scan rate of 0.2 mV per second. Potential vs. Current density plots were then obtained and corrosion rate was calculated by the Tafel extrapolation method.

4.2.5 Hydrogen Embrittlement and micromechanical testing

An electrochemical hydrogen generating cell, connected to a Princeton Advanced Research Potentiostat Model 273A, was set up (Fig. 4.3). The electrochemical hydrogen charging was conducted by utilizing with an Ag/AgCl reference electrode and a Pt counter electrode. For nc Ni films and bulk Ni samples, a 0.1 N H_2SO_4 solution was used as electrolyte.

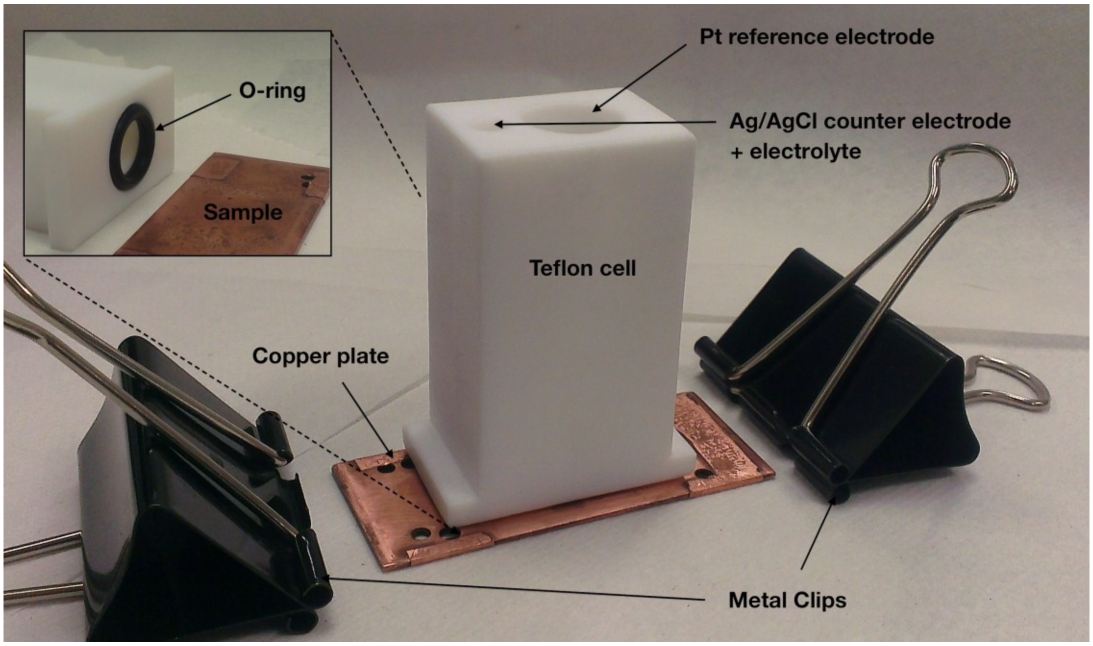

Figure 4.3: *Electrochemical teflon cell for hydrogen charging.*

Fig. 4.3 a shows the Teflon hydrogen charging cell with a copper plate at the bottom, which act as a connection between the potentiostat and sample. As shown in the insert, the sample is placed between the Teflon cell and copper plate and metal clips are used to seal the cell. The Teflon cell has two interconnected orifices on the top that contain the electrolyte and electrodes. The larger orifice opens at the bottom. An O-ring is also placed to seal the electrolyte at the surface of the sample.

The samples were charged with hydrogen in this cell for a set period of time. Immediately after the charging, a microhardness testing machine was used to gauge the effect of HE. Forces of 10 g_f, 25 g_f, 50 g_f and 100 g_f were used to qualitatively characterize surface morphology of tested samples for signs of embrittlement and cracking.

CHAPTER 5

RESULTS AND ANALYSIS

5.1 XRD, SEM and EDS

5.1.1 XRD

Fig. 5.1 shows the X-ray patterns of nc and bulk Ni. Both diffractograms show strong diffraction peaks at 45.5°, 52.1° and 76.9°. These peaks represent the (111), (200) and (220) planes respectively.

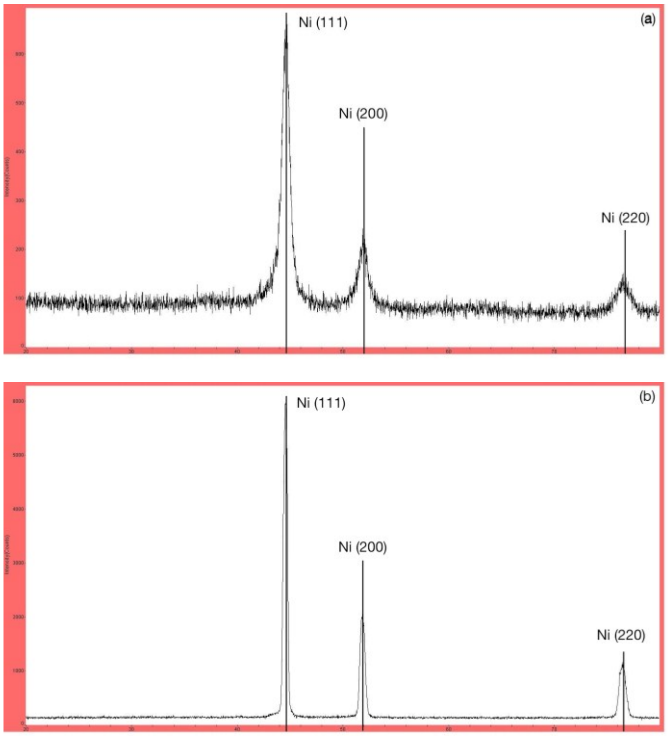

Figure 5.1: *X-ray patterns of (a) nanocrystalline Ni and (b) bulk Ni.*

The (200) and (220) peaks in the nc Ni pattern suggests that it may have a (111) textured structure. The Scherrer formula was used to calculate the grain size.

$$d = \frac{0.94 * \lambda}{0.5B * Cos\theta} \quad Eq.2$$

Bulk Nickel was found to have a grain size of 44 m whereas nc Ni had a grain size of 27 nm.

5.1.2 SEM

Fig. 5.2 shows SEM micrographs of nc Nickel. The micrographs seem to display a grain size larger than that reported by Scherrer analysis of XRD results. However, this method is known to underestimate the grain size [46]. The majority of the grains, as seen from the images, are still sized between 30 and 90 nm.

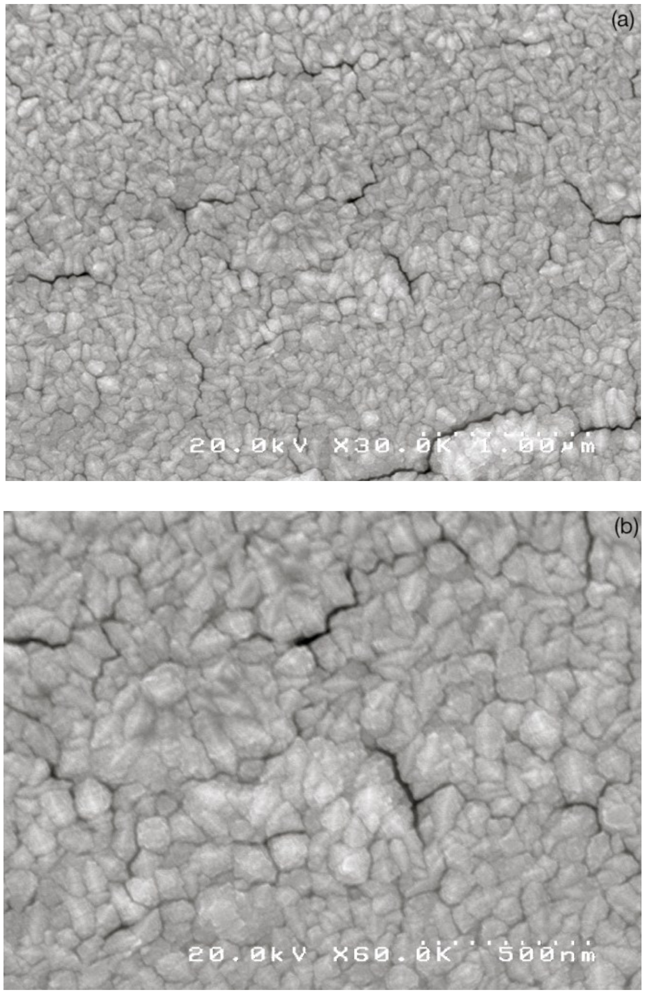

Figure 5.2: *High-resolution SEM micrographs of nc Ni coating at (a) 30k and (b) 60k magnification.*

5.1.3 EDS

Fig. 5.3 gives the EDS spectra of nc and bulk Ni. The spectra show both materials to be relatively pure, with minor amount of contaminants like C and O, which are generally expected. The composition of these materials is described in atomic weight percentages in Table 5.1.

Table 5.1: *Composition of Ni materials* (atomic wt.%).

Material	Ni (wt. %)	C (wt. %)	O (wt. %)	S (wt. %)
Nano Ni	75.96	11.57	12.47	
Bulk Ni	68.28	25.44	5.31	0.97

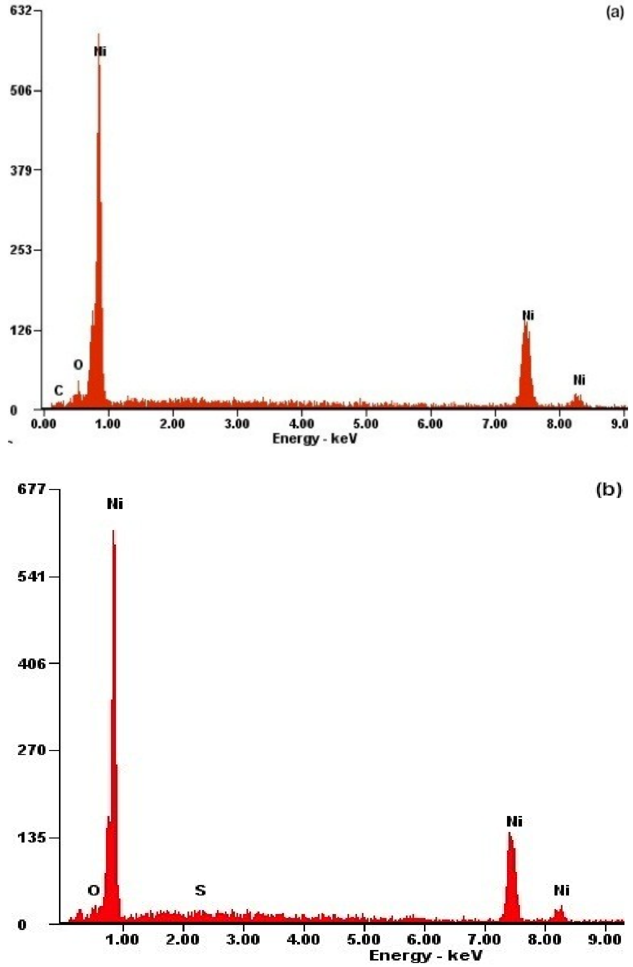

Figure 5.3: *EDS spectra of (a) nanocrystalline and (b) bulk Ni.*

5.2 Corrosion behavior of bulk Nickel

5.2.1 Potentiodynamic polarization behavior in 3.5 % NaCl solution

The reaction of corrosion on the surface of Ni causes a change in the potential of the system from the equilibrium half-cell potential. This is called polarization. When removal of electrons from the metal takes place, the deficiency of electrons causes a positive shift in potential. This is called activation polarization. Current density is considered for Polarization tests because the corrosion rate depends on the amount of current per unit area.

In the case of Nickel, the anodic reaction would be as follows,

$Ni \rightarrow Ni\ 2^{+} + 2e^{-}$ Eq. 3

In presence of oxygen in a neutral solution, the cathodic reaction is,

$O_2 + 2H_2O + 4e^{-} \rightarrow 4OH^{-}$ Eq. 4

The standard reduction potential is +0.82 V vs. Standard Hydrogen Electrode (SHE). However, for a de aerated environment, the cathodic reaction occurs as follows

$2H_2O + 2e^{-} \rightarrow H_2 + 2OH^{-}$ Eq. 5

The standard reduction potential is -0.413 V vs. SHE.

Potentiodynamic polarization tests were conducted on bulk Ni in deaerated conditions, as described in the previous experimental chapter. Fig. 5.4 displays the polarization behavior of bulk Ni in this environment. The activation polarization region tends to dominate the curve and it is similar in shape to previous studies.

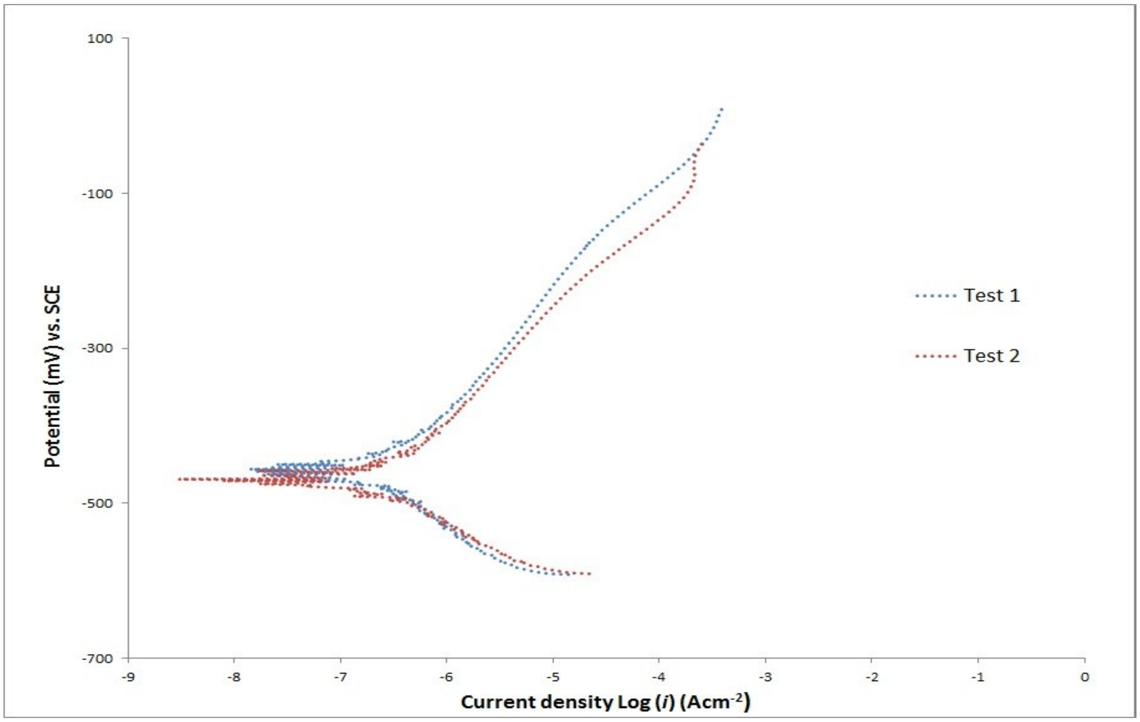

Figure 5.4: *Potentiodynamic behavior of bulk Ni in deaerated 3.5 % NaCl solution.*

Table 5.2: *Potentiodynamic polarization test results of Bulk Ni in deaerated 3.5% NaCl solution.*

Parameter	Test 1	Test 2	Average
Corrosion Potential E_{corr} (mV)	-458.3	-483.2	-470.75
Corrosion rate i_{cor} (µA.cm^{-2})	0.299	0.293	0.296

The corrosion potential and rate can be seen in Table 5.2. The average corrosion potential is around -470 mV and the corresponding corrosion rate is 0.296 µA.cm^{-2}. Exposure to NaCl solution in potentiodynamic conditions does cause corrosion in Ni. Anodic dissolution of Ni begins at around -460 mV. This also is evident from the micrographs below (Fig. 5.5), which show the surface morphology of Ni after the test.

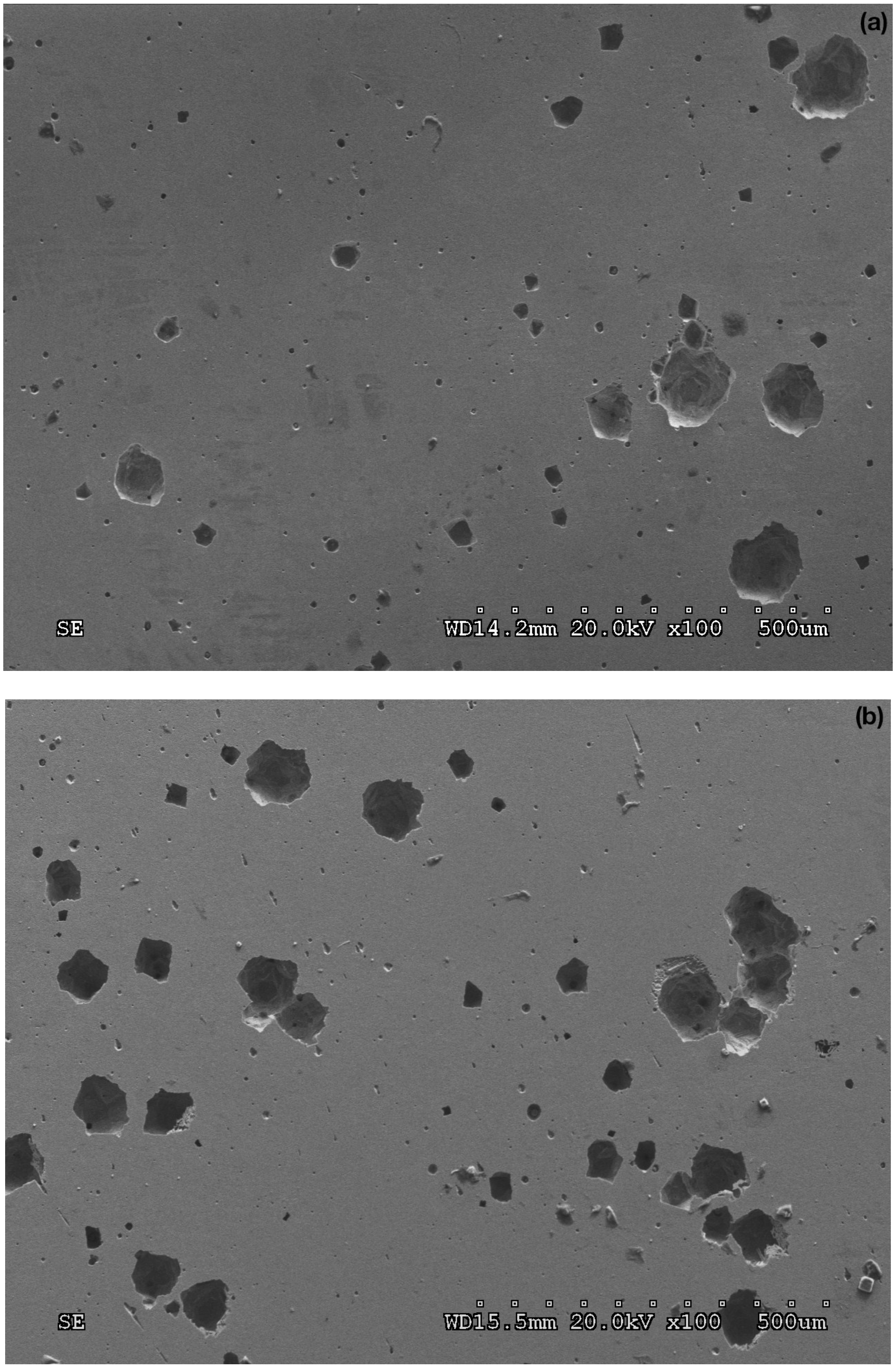

Figure 5.5: *SEM micrographs of bulk Ni surface morphology at different locations (a) and (b), following a potentiodynamic polarization test in deaerated 3.5 % NaCl solution.*

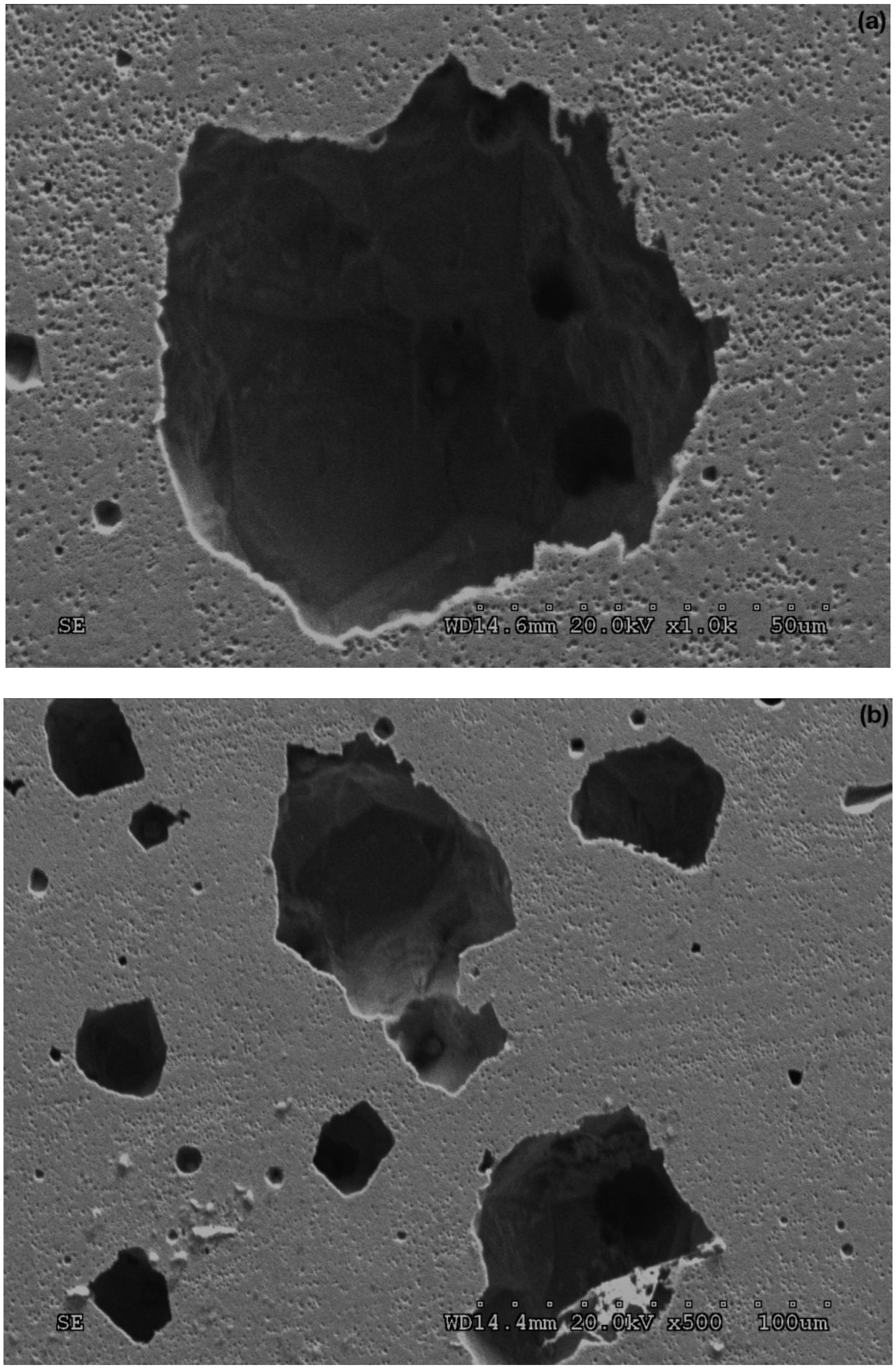

Figure 5.6: *SEM micrographs of Ni surface morphology showing (a) lateral growth and (b) vertical growth of pits on bulk Ni in deaerated 3.5 % NaCl solution.*

Nickel is a corrosion resistant material and this is evident from the low corrosion rate. This can also be seen in the slightly vertical anodic polarization curve, which suggests some passivation. Passivation is the process of forming a thin oxide layer on the exposed surface of a corrosion resistant material during the exposure. The formation of this layer inhibits a further increase in current density with increasing potential. The corrosion occurs in the defects and interruptions in the passive film in the form of pits. It can be seen from micrographs in Fig. 5.5 that initially, numerous small pits are formed of sizes from 5 to 20 μm. This indicated that although there was a passive layer on bulk Ni, it was weak. Some of these pits eventually grow into larger pits that are between 30 and 80 μm. Subsequently, few of these larger pits expand and grow to 100 μm, or more. These pits can grow both laterally and vertically, as seen in Fig. 5.6.

5.2.2 Corrosion potential in 3.5 % NaCl solution

As discussed before, Potential vs. Time measurements are performed to determine the Open Circuit Potential (E_{ocp}) and its variation with time. The E_{ocp} is also called the corrosion potential. At this potential, the system is said to have reached an equilibrium or steady state at which all corrosion reactions are said to occur. These measurements were carried out without external input of power in aerated conditions in both solutions. The results of this test in 3.5 % NaCl solution for bulk Ni samples can be seen in Fig. 5.7.

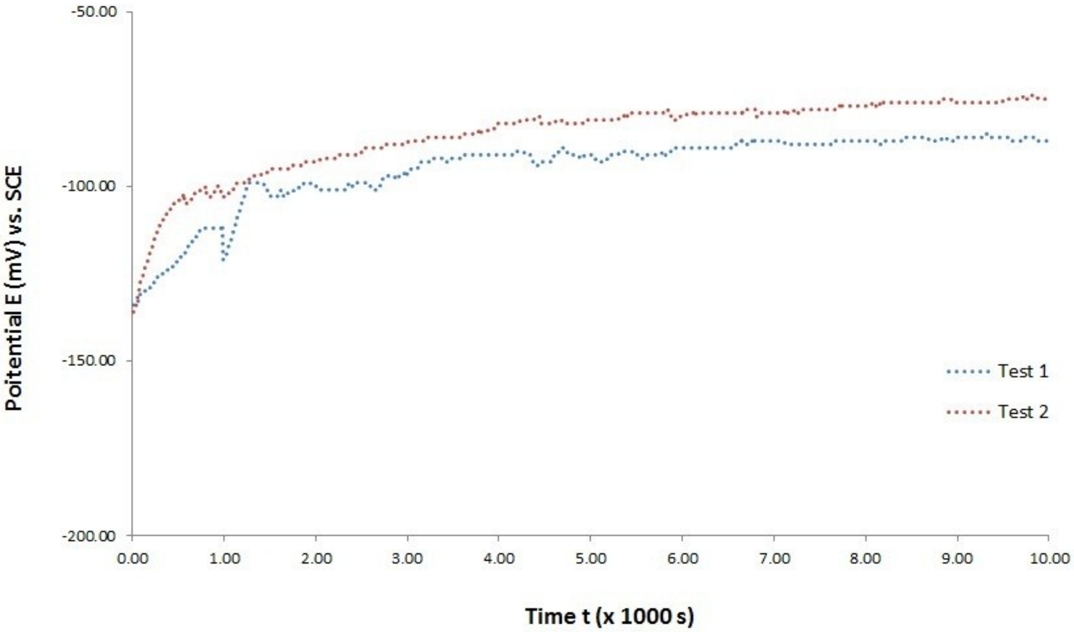

Figure 5.7: *Open circuit potential vs. time measurement results for bulk Ni in aerated 3.5 % NaCl solution.*

The above results indicate that the initial potential of bulk Ni is -381 mV, which then stabilizes to -290 mV. It is to be noted that this potential is higher than the corrosion potential from previous Potentiodynamic polarization experiments. The presence of oxygen causes in the test environment causes the $O_2 + 2H_2O + 2e^- \rightarrow 4OH^-$ reaction to occur; hence increasing the cathodic current density and corrosion rate. Fig. 5.8 shows a typical surface morphology of the bulk Ni sample after the test. Very little pitting is observed as no current or potential is externally applied.

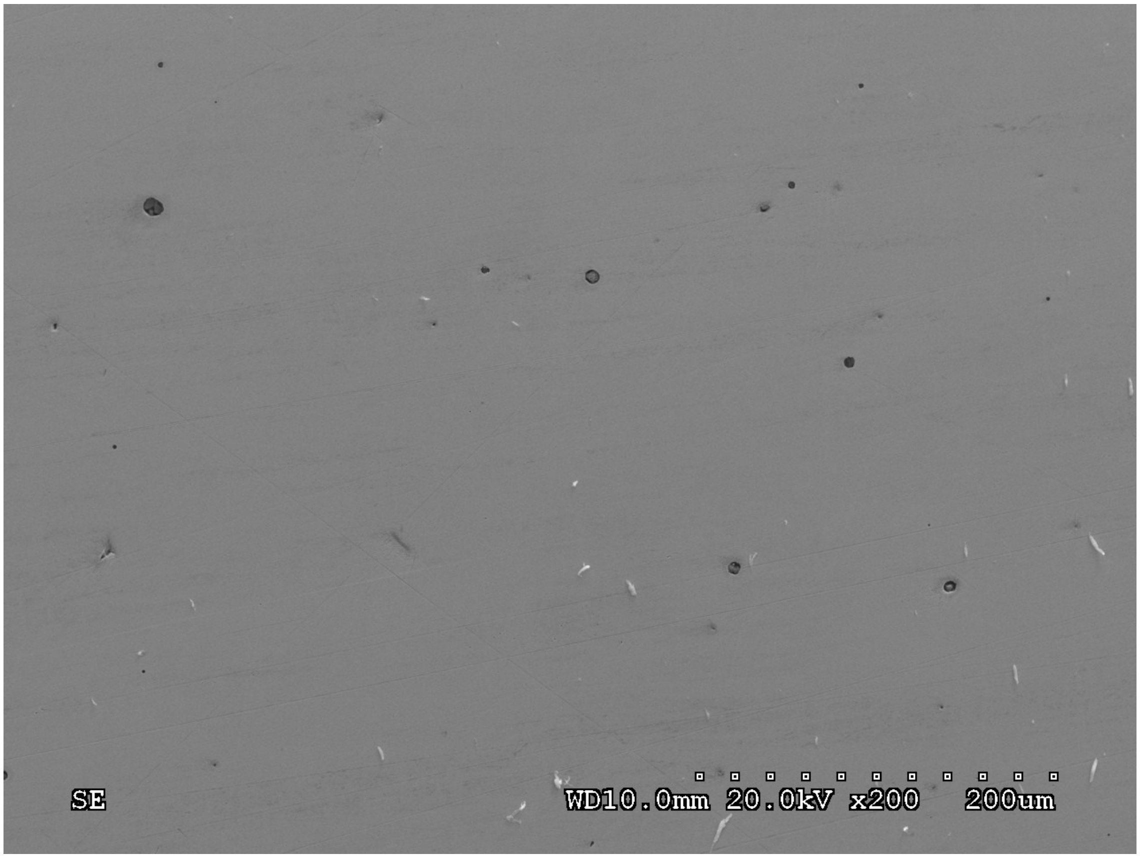

Figure 5.8: *Surface morphology of bulk Ni sample after Open Circuit Potential vs. Time measurement in aerated 3.5 % NaCl solution.*

5.2.3 Potentiodynamic polarization behavior in 0.1 N H_2SO_4 solution

Potentiodynamic polarization tests were performed with 0.1 N H_2SO_4 solution in a de aerated environment in the same experimental set up as discussed previously. The results of these tests can be seen in Fig. 5.9 and Table 5.3.

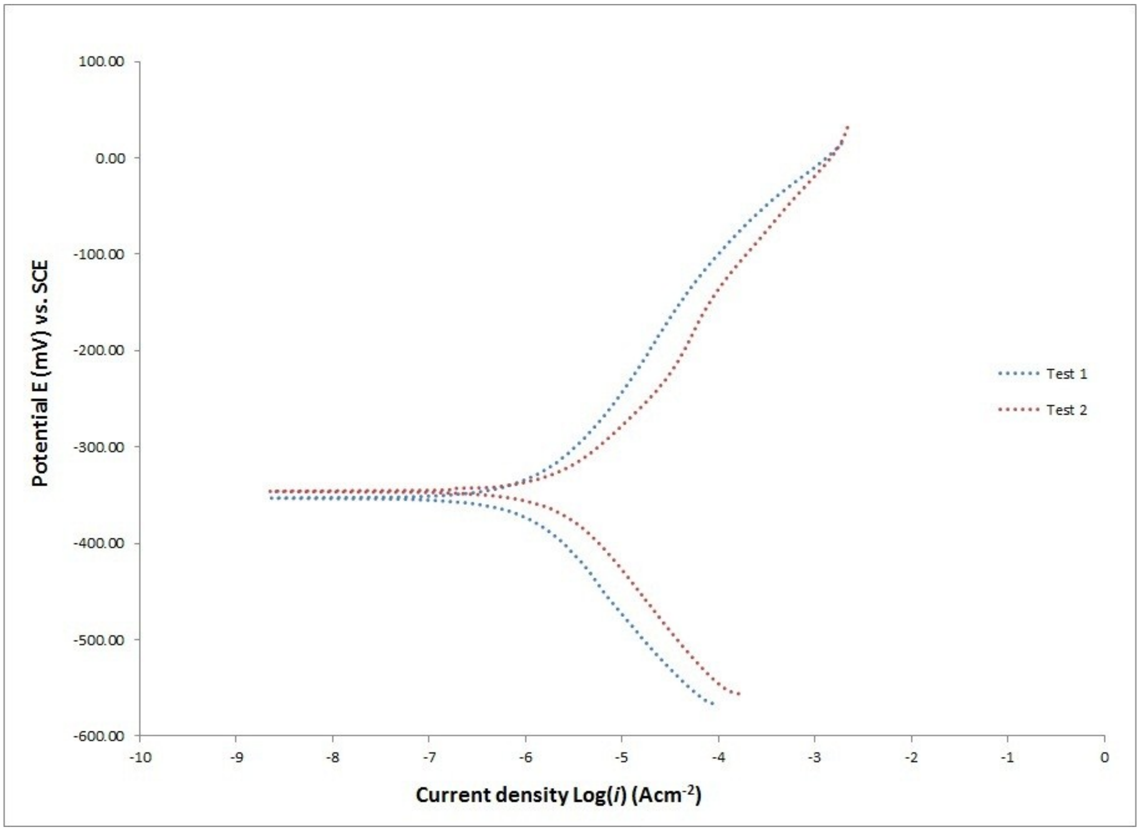

Figure 5.9: *Potentiodynamic behavior of bulk Ni in deaerated 0.1 N deaerated H_2SO_4 solution.*

Table 5.3: *Potentiodynamic polarization test results of Bulk Ni in 0.1 N deaerated H_2SO_4 solution.*

Parameter	Test 1	Test 2	Average
Corrosion Potential E_{corr} (mV)	-346.10	-353.20	-349.65
Corrosion rate i_{cor} (μA.cm^{-2})	3.137	1.474	2.310

From the results, it is evident that anodic dissolution of Ni begins around -350 mV. The solution used in the experiment has a very low pH of 2.2 and no passive film is formed for this solution. This is predicted by the Pourbaix diagram (Fig. 3.11), where no passive film is present for Ni in very acidic solutions. The average corrosion rate for these experiments was 2.31 μA.cm^{-2}. This rate is much higher than the corrosion rate in the 3.5 % NaCl solution. Fig. 5.10

reveals the surface morphology of bulk Ni after the potentiodynamic test. Fig. 5.10 reveals no pitting and indicates uniform dissolution of the sample.

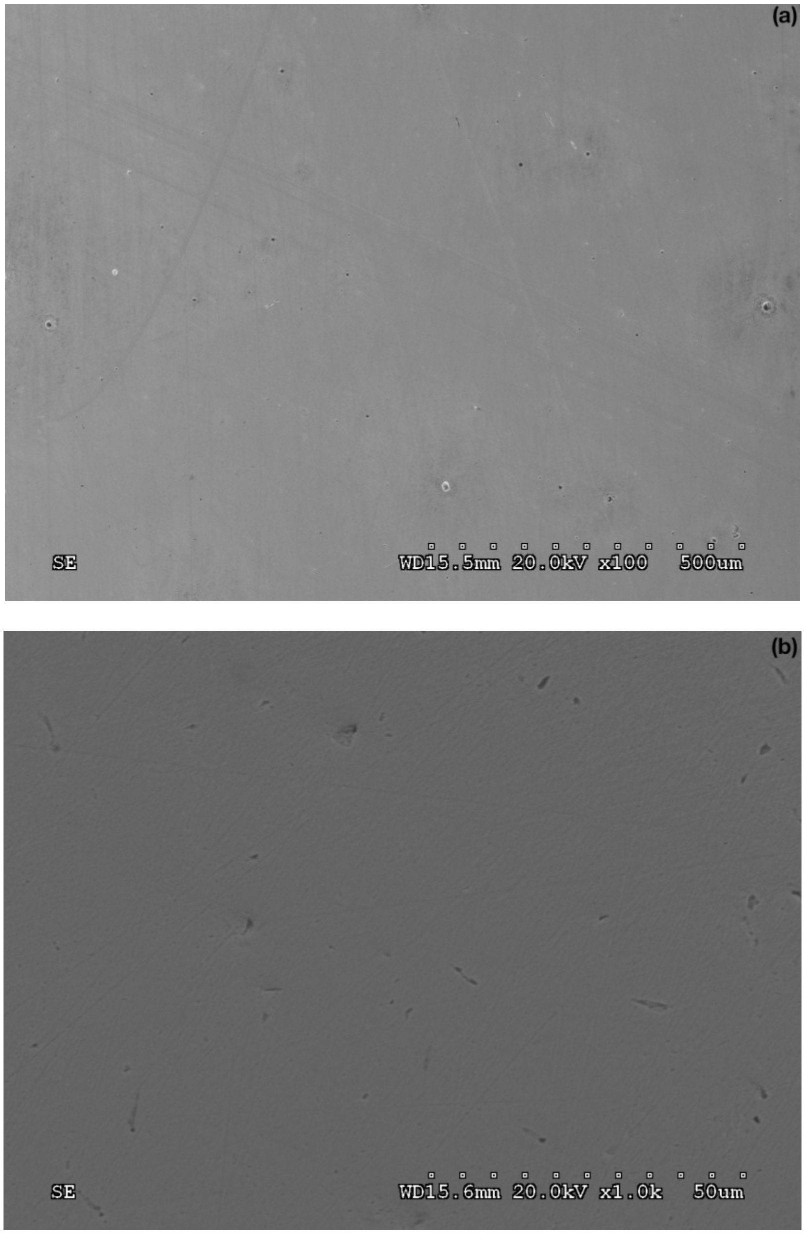

Figure 5.10: *SEM micrographs of bulk Ni surface morphology at (a) low magnification and (b) high magnification following a potentiodynamic polarization test in deaerated 0.1 N* H_2SO_4 *solution.*

5.2.2 Corrosion potential in 3.5 % NaCl solution

Fig. 5.11 displays the results of Potential vs. Time measurements. The potential is seen to rise a little initially but stabilizes at -260 mV. This is more anodic than previous Potential vs. Time measurement in 3.5 % NaCl solution due to the lack of passive behavior of Ni in 0.1 N H_2SO_4. These results are seen consistent for all tests. Fig. 5.12 shows the surface morphology of bulk Ni. Apart from the small pits, the surface is largely featureless.

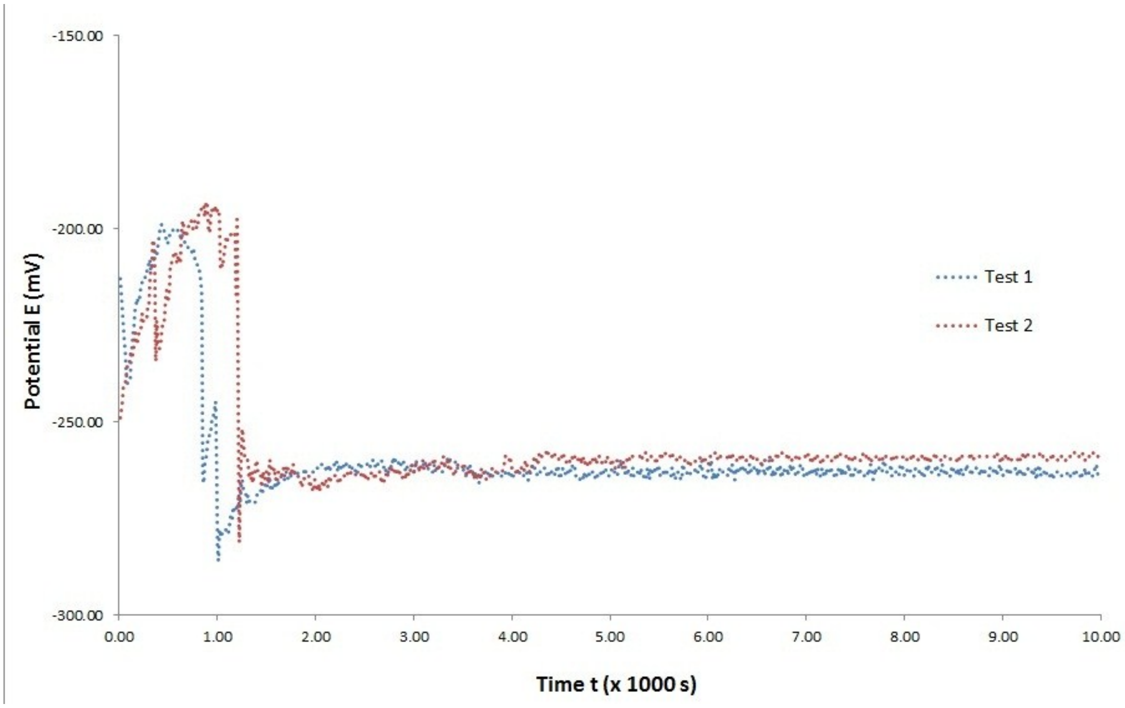

Figure 5.11: *Open circuit potential vs. time measurement results for bulk Ni in aerated 0.1 N H_2SO_4 solution.*

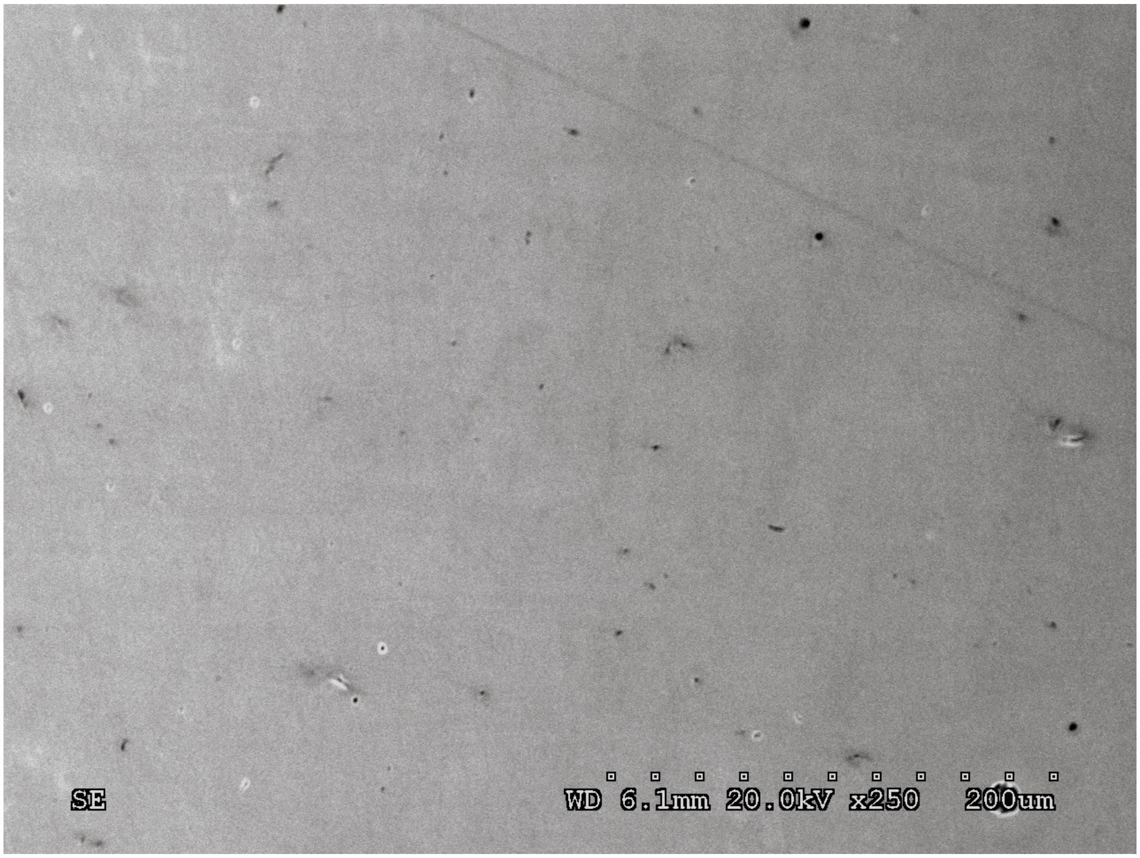

Figure 5.12: *Surface morphology of bulk Ni sample after open circuit potential vs. Time measurement in aerated 0.1 N* H_2SO_4 *solution.*

5.3 Corrosion behavior of nanocystalline Nickel

5.3.1 Potentiodynamic polarization behavior in 3.5 % NaCl solution

Fig. 5.13 presents the results for the potentiodynamic polarization tests in deaerated 3.5 % NaCl solution. These results are further tabulated in Table 5.4. It is evident that nc Ni has a more anodic corrosion potential of around -230 mV, as compared to -360 mV for bulk Ni. However, the results also reveal a distinct active-passive behavior. The samples were tested up to 800 mV above corrosion potential. Unlike bulk Ni, the nc Ni coating displays passivation from a potential of roughly -200 mV to around -440 mV, after which it starts to show activation. The nc Ni also has a lower corrosion rate of 0.11 μA.cm^{-2}, as compared to the 0.3 μA.cm^{-2} for bulk Ni.

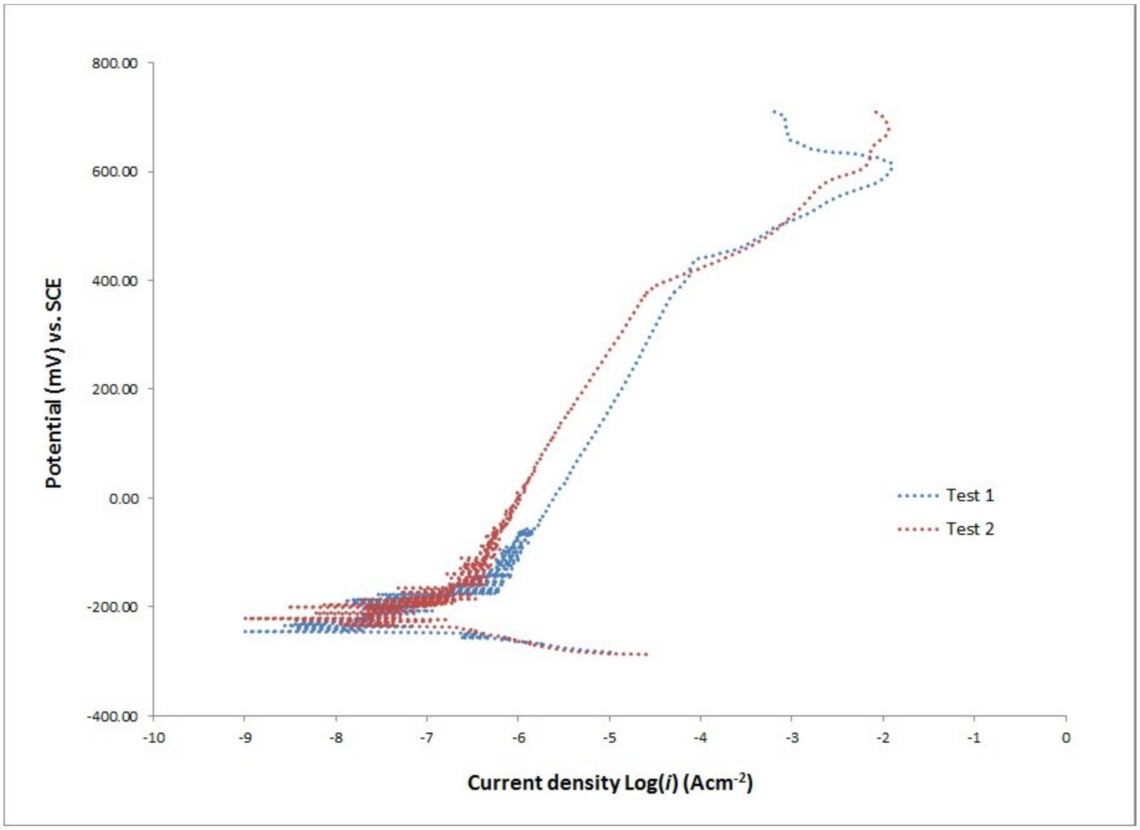

Figure 5.13: *Potentiodynamic behavior of nc Ni in deaerated 3.5 % NaCl solution.*

Table 5.4: *Potentiodynamic polarization test results of nc Ni coating in 3.5 % deaerated NaCl solution.*

Parameter	Test 1	Test 2	Average
Corrosion Potential E_{corr} (mV)	-232.1	-222.7	-227.4
Corrosion rate i_{corr} (μA.cm^{-2})	0.18	0.04	0.11

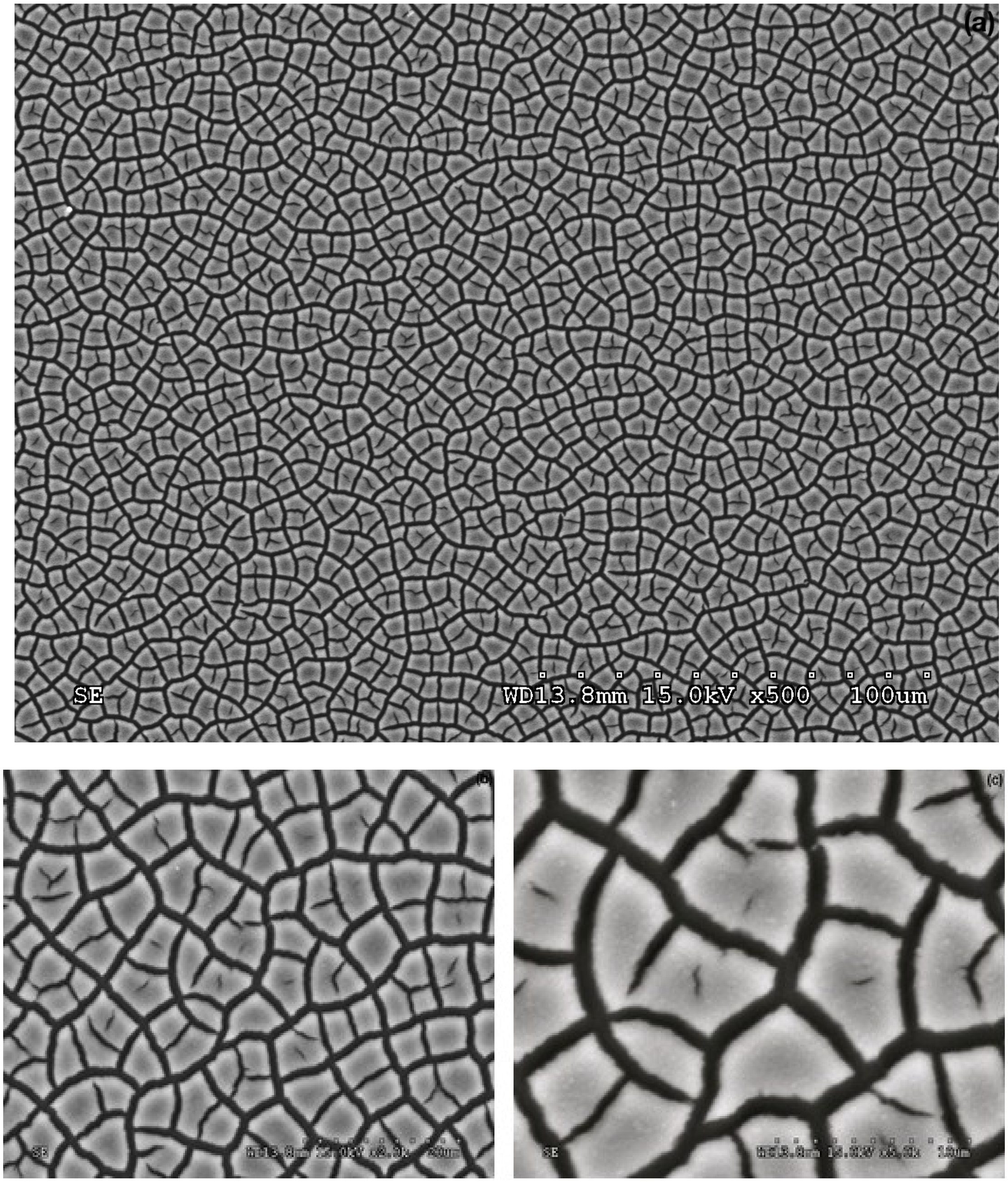

Figure 5.14: *Surface morphology of nc Ni film exposed to potentiodynamic testing in deaerated 3.5 % NaCl solution at (a) low magnification, (b) high magnification and (c) division of Ni domains due to corrosion.*

Fig. 5.14a reveals the surface morphology of the nc Ni coating after the potentiodynamic test. The coating appears to have corroded uniformly across the surface, without formation of pits. The structure of the corroded coating looks like a network of “cells” divided by a “mesh” of corrosion. From the micrographs, prominent grain boundaries and triple junctions seem to have been the subject of the corrosion attack. These numerous defects help to produce a consistent passive layer, which is seen in the results above. Fig. 5.14b reveals the structure at a higher magnification. This micrograph suggests a trend that once the prominent grain boundaries are corroded, corrosion spreads to lesser grain boundaries and keeps dividing the “cells” of Nickel.

The reason behind this type of corrosion is the presence of numerous grain boundaries and triple junctions, due to the significantly smaller grain size of the coating. These grain boundaries and triple junctions in the structure of the coating are preferential sites for corrosion. Such a structure spreads out the total cathodic current density applied to the sample to the numerous sites and hence reduces the intensity of corrosion. This results in a more uniform degradation and discourages pit formation.

To better assess the corrosion behavior of the nc Ni film, one potentiodynamic test was stopped prematurely in the passivation region of anodic polarization in order to examine structure. Fig. 5.15 shows micrographs of the surface morphology of this film.

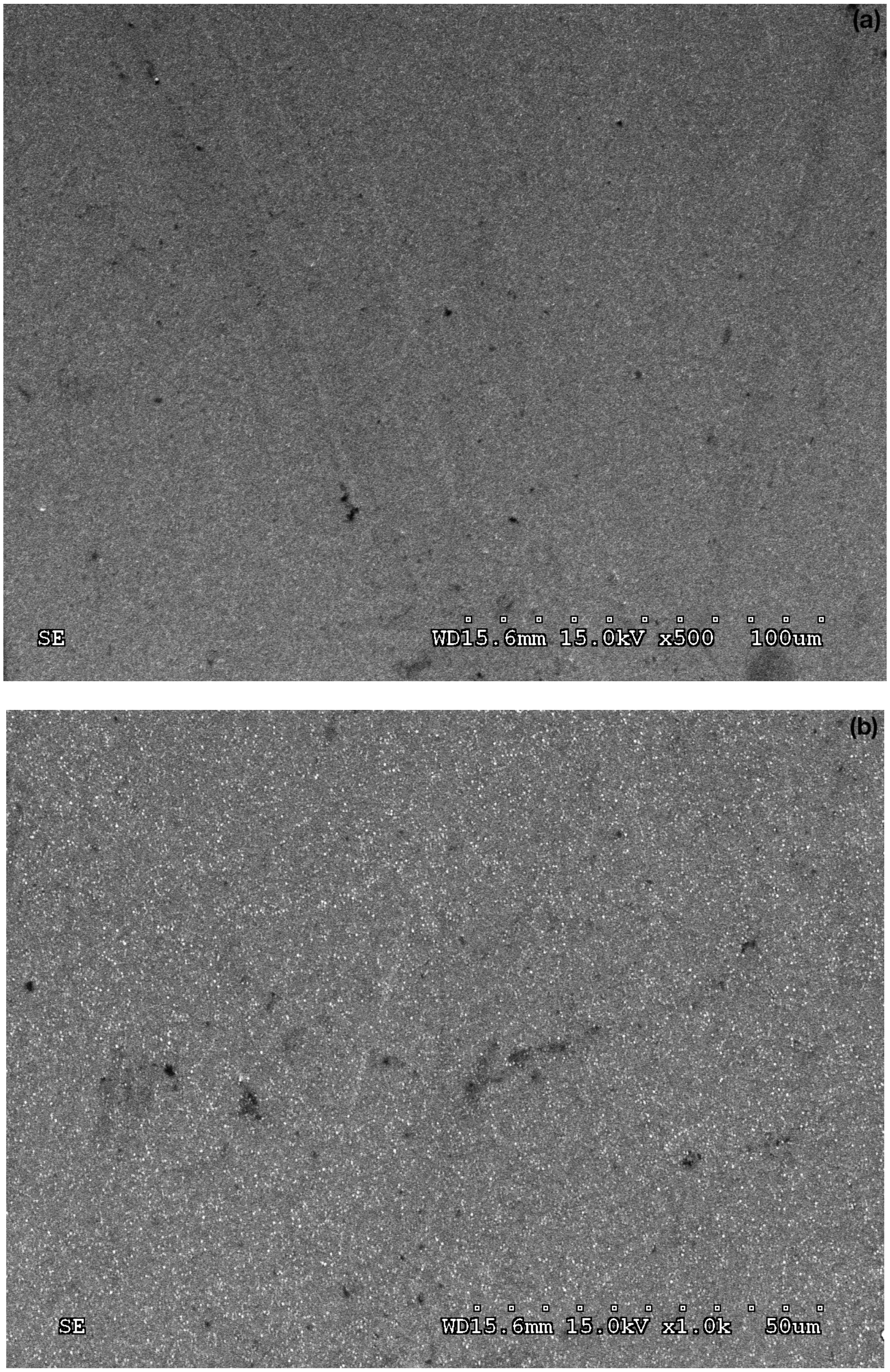

Figure 5.15: *SEM micrographs of surface morphology of nc Ni coating at (a) low and (b) high magnification, after incomplete potentiodynamic polarization test in deaerated 3.5 % NaCl solution.*

5.3.2 Corrosion potential in 3.5 % NaCl solution

Corrosion potential vs. time experiments were carried out in aerated 3.5 % NaCl solution for nc Ni samples. The initial -135 mV potential eventually reaches equilibrium at around -80 mV. This rise in equilibrium potential can again be attributed to the presence of oxygen. As discussed previously, oxygen introduces another cathodic reaction, increases the cathodic current density and corrosion rate as well. The results to the corrosion potential vs. time experiments can be seen in Fig. 5.16.

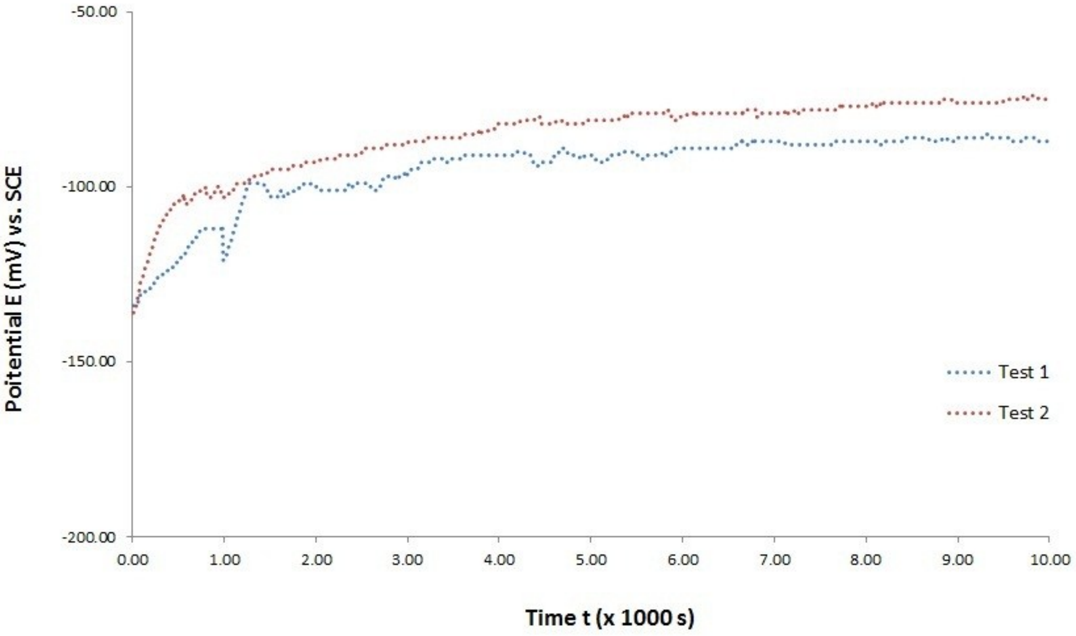

Figure 5.16: *Open circuit potential vs. time measurement results for nc Ni in aerated 3.5 % NaCl solution.*

Fig. 5.17 shows the surface morphology of the nc coating after the test. The coating surface appears to be featureless for the most part. This indicates that passivation without any corrosion attack is present at the passive potential range.

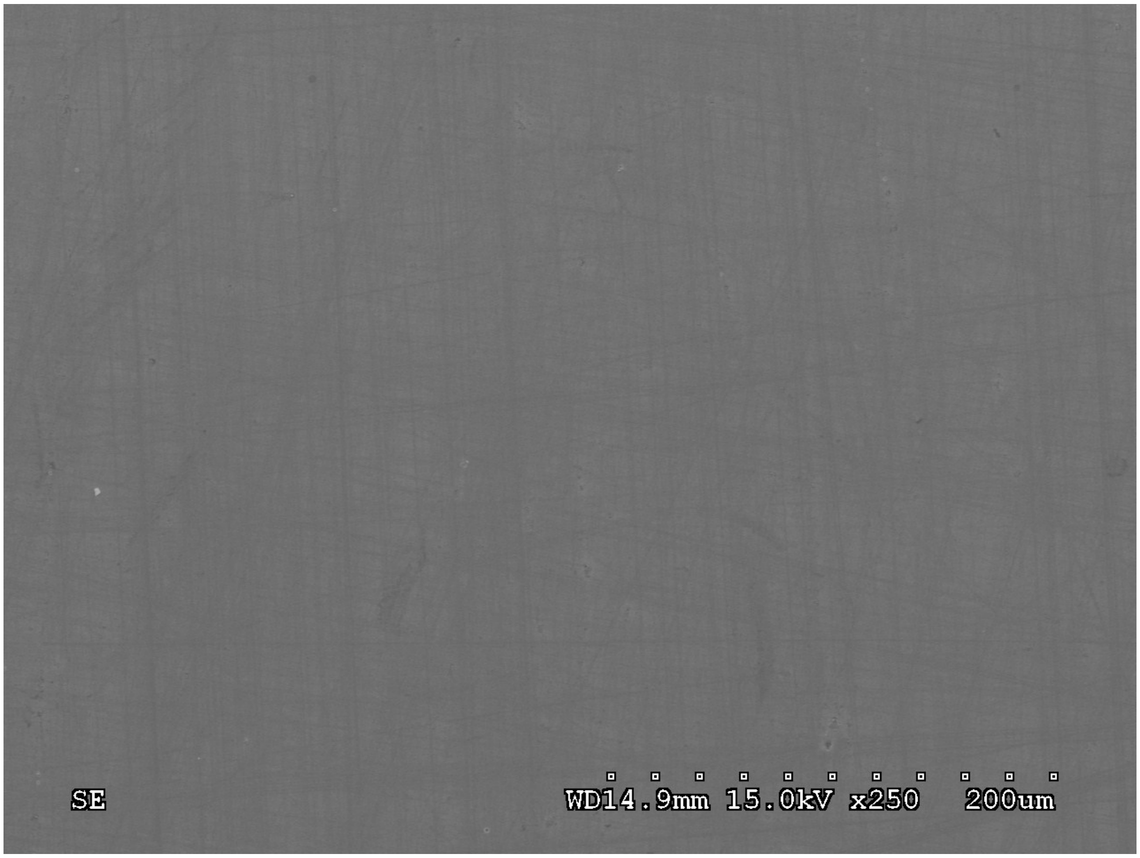

Figure 5.17: *Surface morphology of nc Ni sample after open circuit potential vs. time measurement in aerated 3.5 % NaCl solution.*

5.3.3 Potentiodynamic polarization behavior in 0.1 N H_2SO_4 solution

Similar to bulk Ni, potentiodynamic polarization tests were carried out on nc Ni coatings in deaerated 0.1N H_2SO_4 solution. The results can be seen in Fig. 5.18 and Table 5.5.

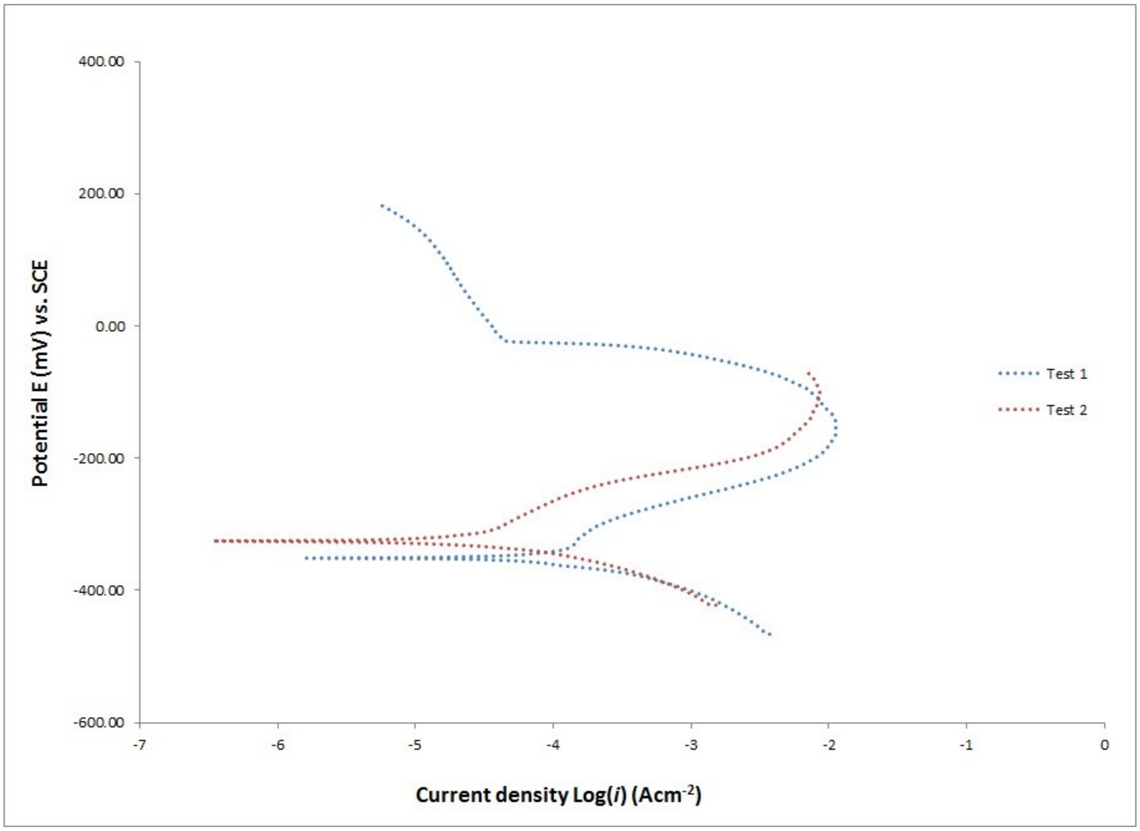

Figure 5.18: *Potentiodynamic behavior of nc Ni in 0.1N H_2SO_4 deaerated solution.*

Table 5.5: *Potentiodynamic polarization test results of nc Ni in 0.1 N deaerated H_2SO_4 solution.*

Parameter	Test 1	Test 2	Average
Corrosion Potential E_{corr} (mV)	-350.7	-325.2	-327.95
Corrosion rate i_{cor} (μA.cm^{-2})	87.78	18.27	53.025

Like bulk Ni, nc Ni samples show pure anodic behavior. The corrosion begins at about -327 mV for nc Ni samples, which is close to the -350 mV for bulk Ni. However, nc Ni shows a much higher corrosion rate of 53.00 μA.cm^{-2}, as compared to the rate of 2.31 μA.cm^{-2} for bulk Ni.

For Test 1, after the anodic curve for the nc Ni ends, another corrosion curve emerges. After the surface is depleted of Ni, the Cr layer underneath is exposed to the 0.1 N H_2SO_4.

The above tests suggest that a nc structure is detrimental to corrosion resistance, if the material is exposed to an environment where it does not passivate. In this case, the increase in grain boundaries in the nc structure promotes the hydrogen reaction and increases the cathodic current density; which in turn increases the corrosion rate.

Fig. 5.19 shows the surface morphology of the nc Ni coating from Test 2 that was tested up to -155 mV. It is expected that significant dissolution of the coating has taken place, but still has stable Ni film. This is confirmed from the periodic and uniform corrosion “mesh” seen in Fig. 5.19. This structure is similar to previous observations for potentiodynamic tests in 3.5 % NaCl solution, except the Ni cells are smaller and more divided. This indicates the higher extent of dissolution due exposure to the very active 0.1 N $H2_{S}O_4$ solution.

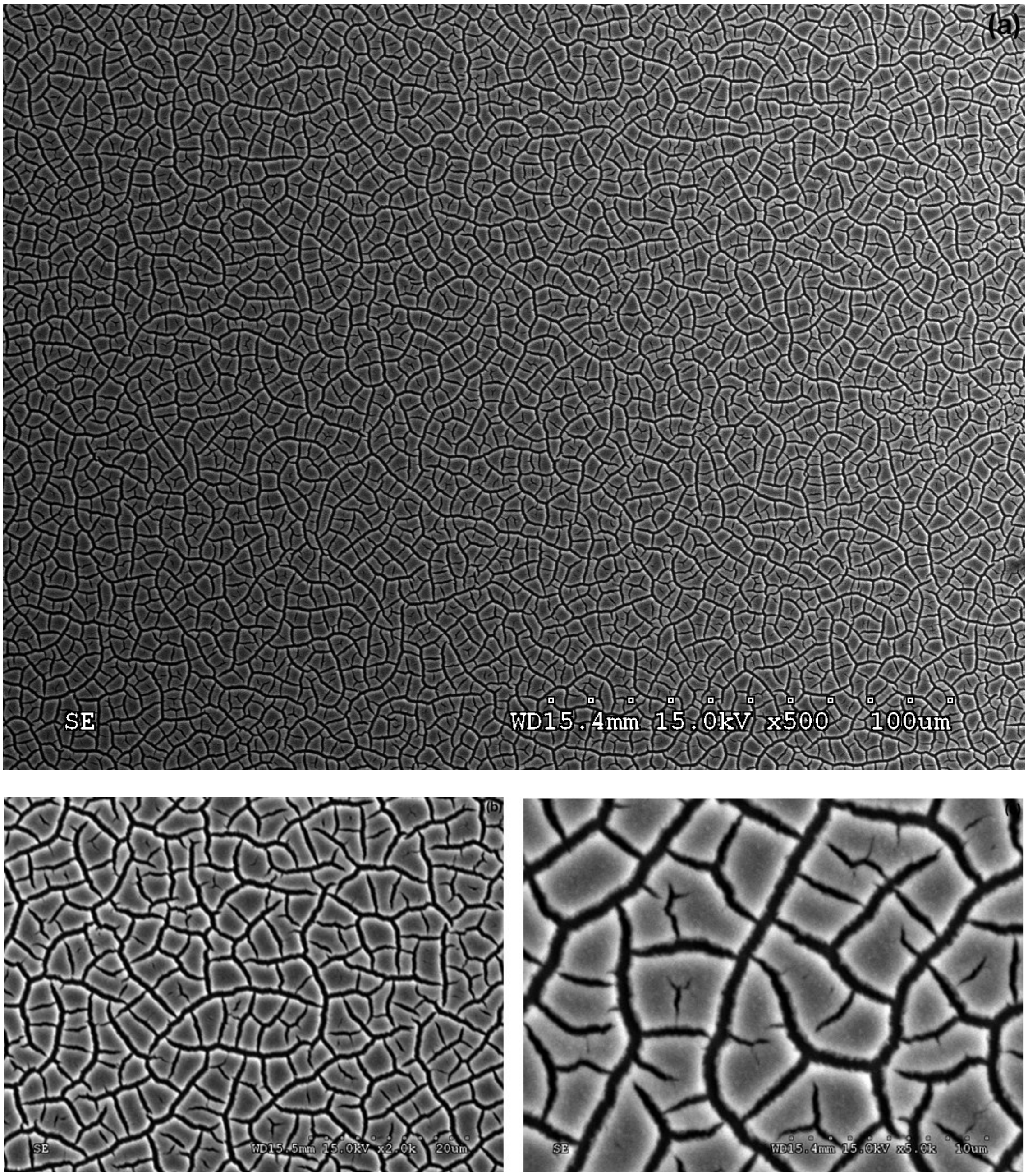

Figure 5.19: *Surface morphology of nc Ni film exposed to potentiodynamic testing in deaerated 0.1N* H_2SO_4 *solution at (a) low magnification, (b) high magnification and (c) fine division of Ni domains due to corrosion.*

5.3.3 Corrosion potential in 0.1 N H_2SO_4 solution

Fig. 5.20 shows the test results for open circuit potential vs. time measurements for nc Ni coatings in aerated 0.1 N H_2SO_4 solution. The initial potential of around -200 mV stabilizes around -350 mV.

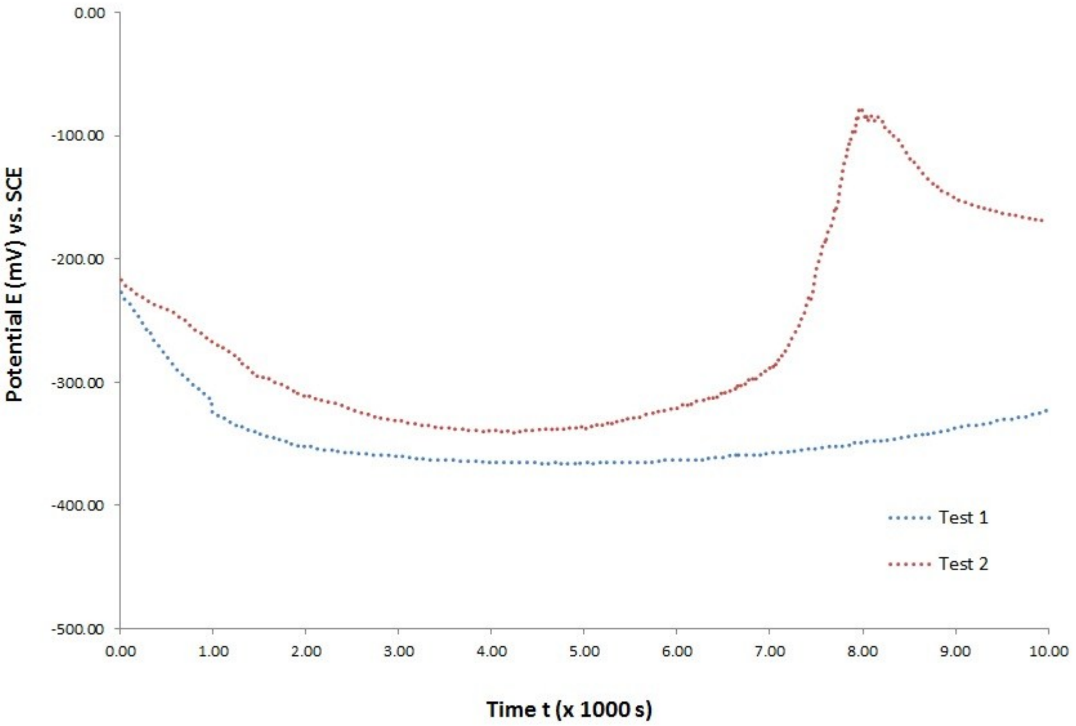

Figure 5.20: *Open circuit potential vs. time measurement results for nc Ni in aerated 0.1 N H_2SO_4 solution.*

After stabilizing, the potential rises again slightly in Test 1 and significantly so in Test 2. This is attributed to the very active nature of the 0.1 N H_2SO_4 solution. Exposing nc Ni films to such environment for a long period of time causes significant dissolution of the film in Test 1 (Fig. 5.21); and total dissolution of the film in Test 2 (Fig. 5.22). This is also corroborated by EDS results after the tests (Fig.5.23)

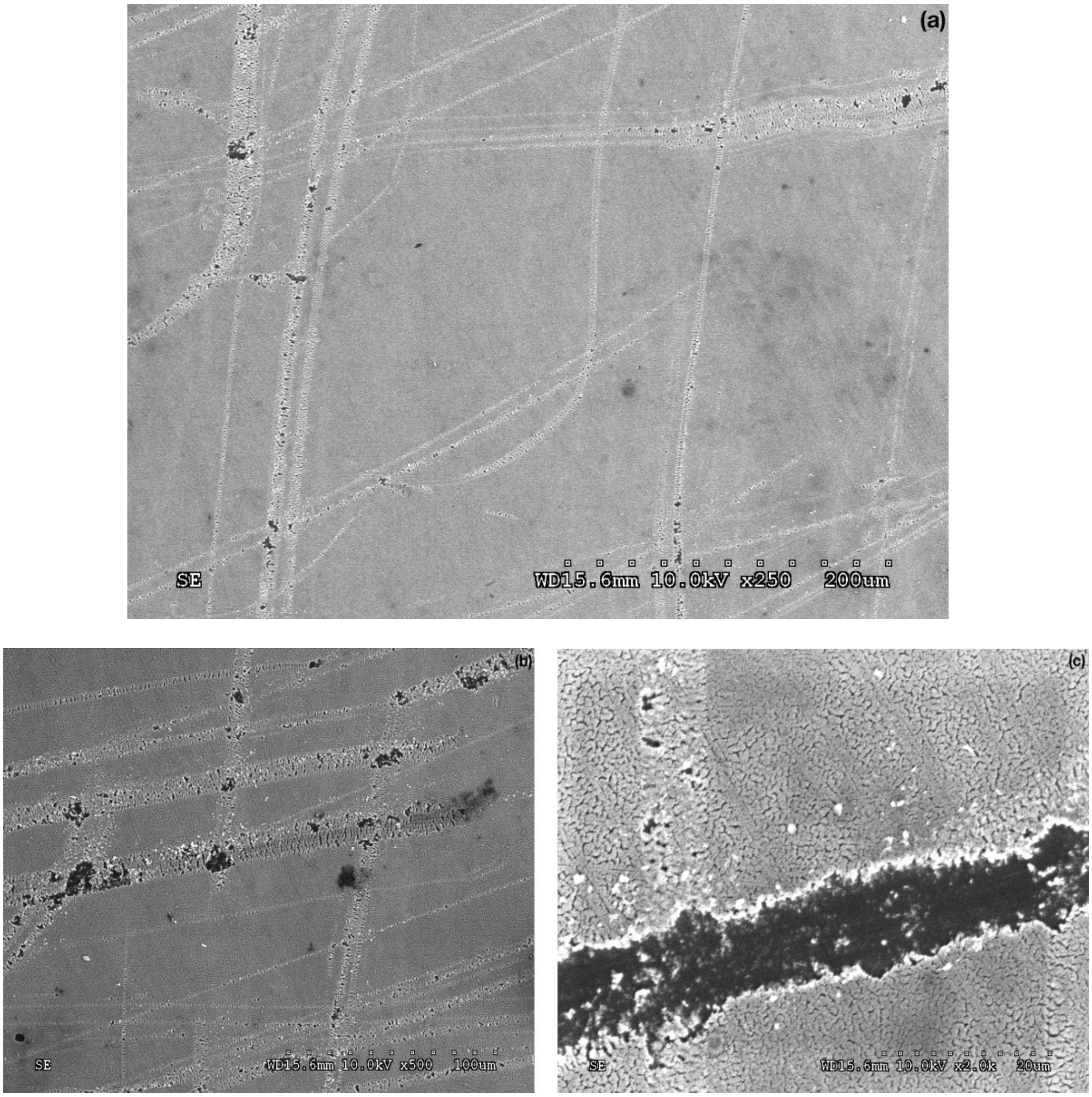

Figure 5.21: *Surface morphology of nc Ni sample after Test 1 for open circuit potential vs. time measurement in aerated 0.1 N H_2SO_4 solution.*

Fig. 5.21a shows the morphology of the nc Ni sample after Test 1. It is evident that significant dissolution has taken place from Fig. 5.21b and 5.21c, where the Ni film has given way to the Si substrate. Fig. 5.21 shows the surface morphology of the nc Ni sample after Test 2. The surface appears to be featureless and is not expected to have any Ni. This is corroborated by EDX analysis shown in Fig. 5.23 and Table 5.6. The spectra reveal the absence of Ni coating on the surface.

Figure 5.22: *Surface morphology of nc Ni sample after open circuit potential vs. time measurement in aerated 3.5 % NaCl solution.*

Table 5.6: *Composition of nc Ni sample after after open circuit potential vs. time measurements in 0.1 N H_2SO_4 solution.*

Si (wt. %)	S (wt. %)	Cr (wt. %)	C (wt. %)	O (wt. %)
73.42	0.20	3.91	11.28	11.19

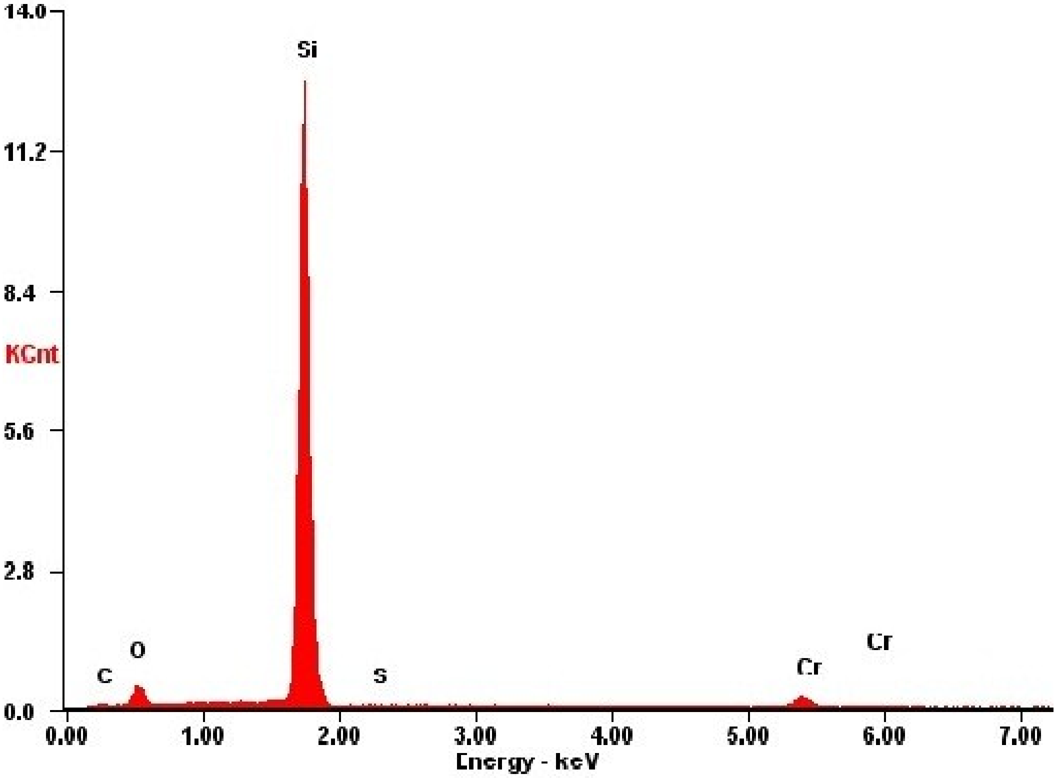

Figure 5.23: *EDS spectra of nc Ni sample after open circuit potential vs. time measurements in 0.1 N H_2SO_4 solution.*

5.4 Hydrogen Embrittlement of bulk Nickel

As discussed in the – 1V potential below Open Circuit Potential was applied to the system to drive the electrochemical reaction in cathodic region to avoid dissolution of Ni sample. No external stirring was applied, meaning the rate of reaction was diffusion controlled. Table 5.7 reports the charge applied during the electrochemical reaction for bulk and nc Ni. Experimental section, a three electrode electrochemical set up was used with an Ag/AgCl reference electrode, Pt counter electrode and 0.1 N H_2SO_4 electrolyte. The sample was placed in this Teflon cell to induce adsorption of hydrogen into its microstructure.

Table 5.7: *Experimental conditions for electrochemical hydrogen charging for bulk and nc Ni.*

Material	Test #	Time (s)	Charge applied (C)
bulk Ni	1	10800	98.00
	2	10800	53.80
nc Ni	1	7200	13.55
	2	7200	24.50

Following the electrochemical charging of hydrogen, the samples were immediately transferred to a microhardness testing machine and indented to observe change in surface morphology near the indents. A change in surface morphology near the indent was observed for 50 g_f loads in hydrogen-charged Ni samples. Fig. 5.24a shows an example of a clean indentation as observed for standard bulk Ni samples. Fig. 5.24b is the surface morphology of the bulk Ni sample after 3 hours of electrochemical charging. The surface at the sharpest corner of the indentation appears to display slip, which can be induced by the presence of hydrogen.

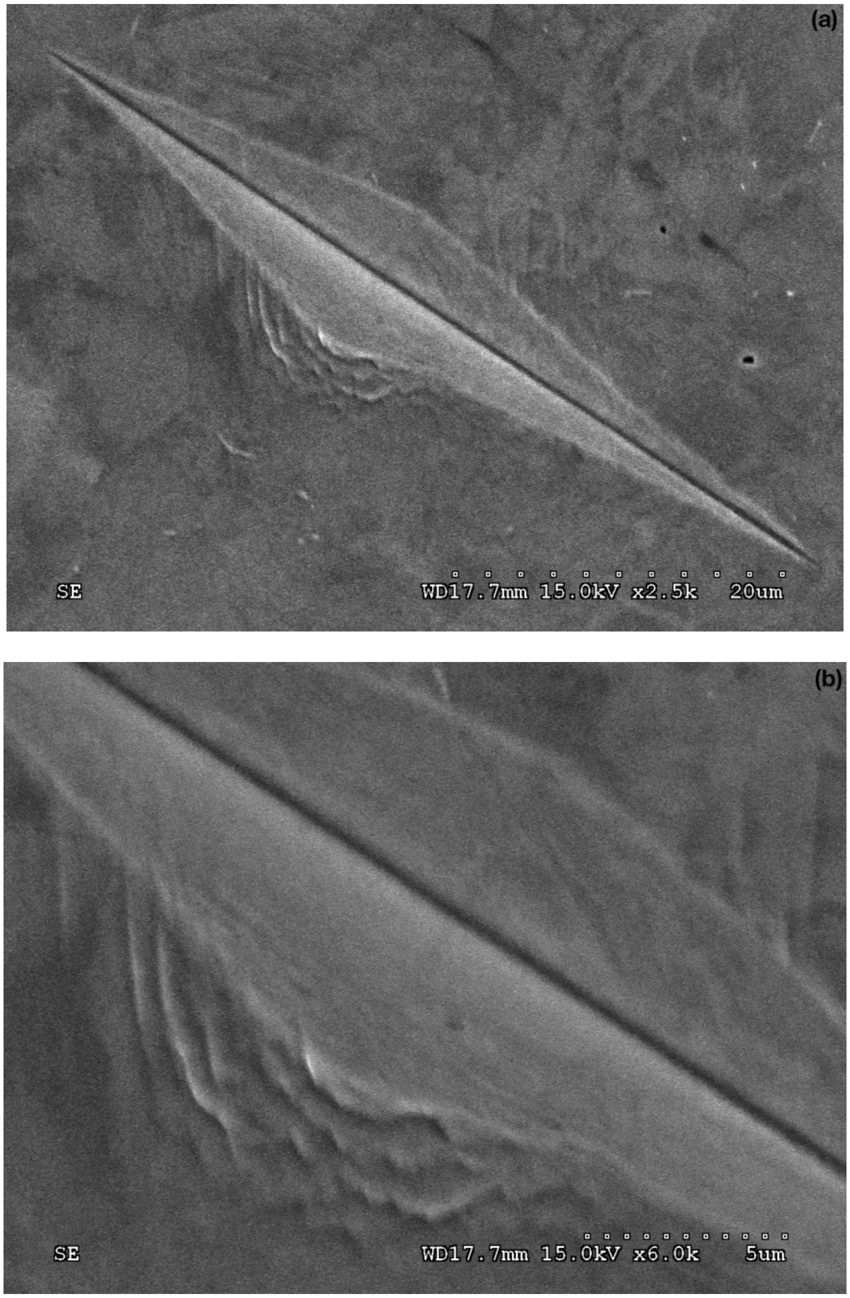

Figure 5.24: *Surface morphology of bulk Ni near 50 g_f microhardness indentation (a) after hydrogen charging and (c) magnified hydrogen induced slip at indent corner.*

The microhardness is measured by the dimensions of the indentation. The microhardness measurements hold true in the case of standard and embrittled bulk Ni samples, as the indentation shape is more or less intact. The hardness results reveal a slight increase in the hardness for Ni samples that were charged with hydrogen (Table 5.8).

Table 5.8: *Microhardness measurements in GPa for standard bulk Ni and hydrogen-charged bulk Ni samples.*

Sample	1	2	3	4	5	Average
Standard bulk Ni (GPa)	1.687	2.01	1.844	1.834	1.893	1.85
Hydrogen-charged bulk Ni (GPa)	2.236	1.961	2.118	2.177	2.123	2.123

These results indicate an onset of increased hardness but do not display overt nature of HE, like cracking. The slight increase in hardness is attributed to the presence of H that causes local hardening.

5.5 Hydrogen Embrittlement of nanocrystalline Nickel

Electrochemical hydrogen charging of nc Ni samples was conducted in a similar way, as discussed previously. However, charging of nc Ni was performed for 2 hours, instead of 3 hours in 0.1 N H_2SO_4 solution.

After hydrogen charging, the samples were immediately transferred to the microhardness instrument to observe surface morphology near indentations. 10, 25, 50 and 100 g_f forces were applied. Although 10 g_f forces do not show any signs of embrittlement, 25, 50 and 100 g_f load settings cause noticeable cracks in the nc coating.

Fig. 5.25 shows the surface morphology of a 25 g_f indentation on hydrogen charged nc Ni coating. It is evident that the film has failed in a brittle fashion, by buckling and spalling on one side of the indentation. No plastic deformation is seen in these indents, as expected from ductile materials like Ni. This trend is also noticed in higher loads of 50 and 100 g_f, as shown in Fig. 5.26 and Fig. 5.27, respectively.

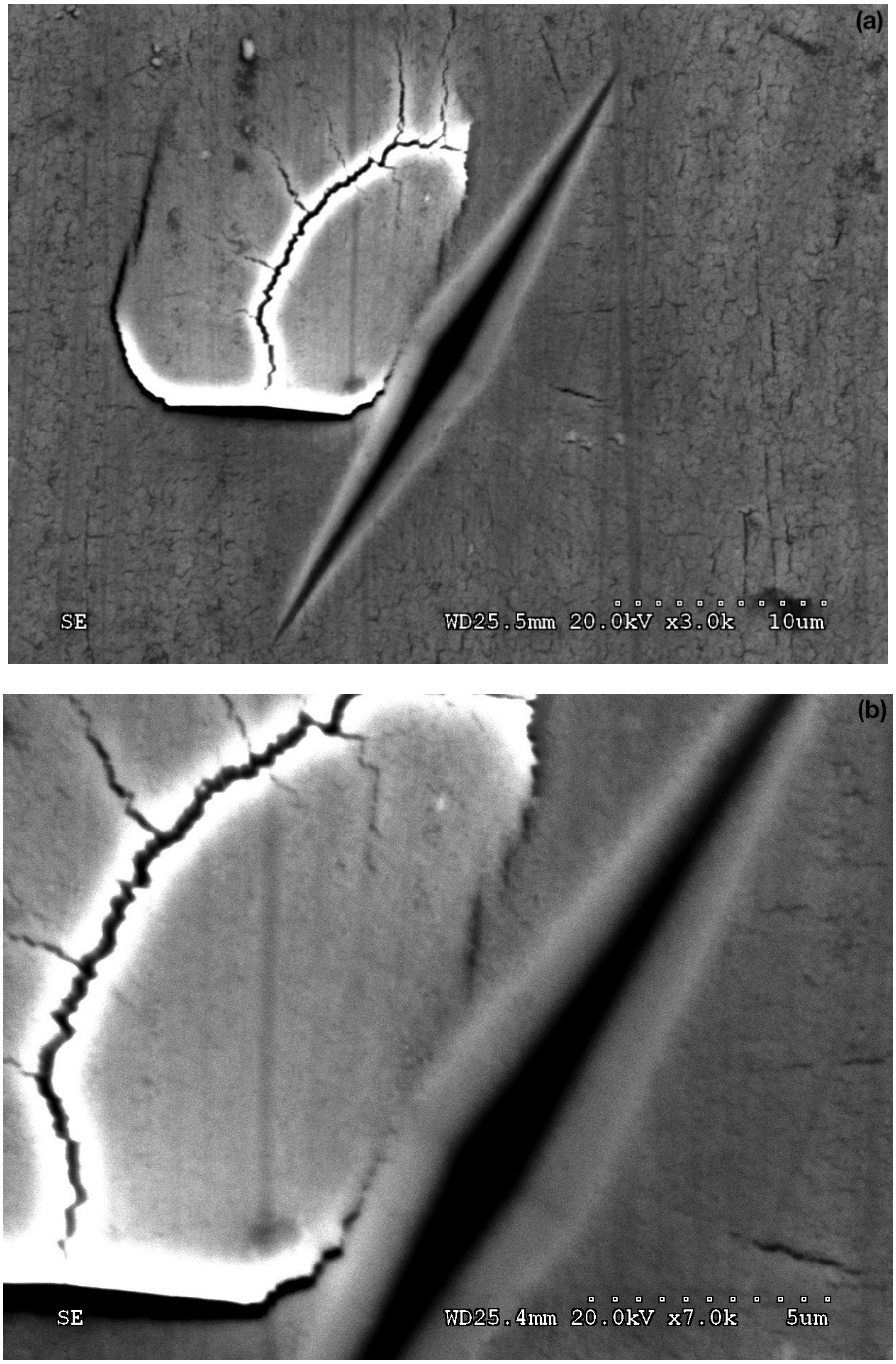

Figure 5.25: *Surface morphology of nc Ni film near 25* g_f *indentation after hydrogen charging at (a) low magnification and (b) buckling, spalling and radial cracks in film at high magnification.*

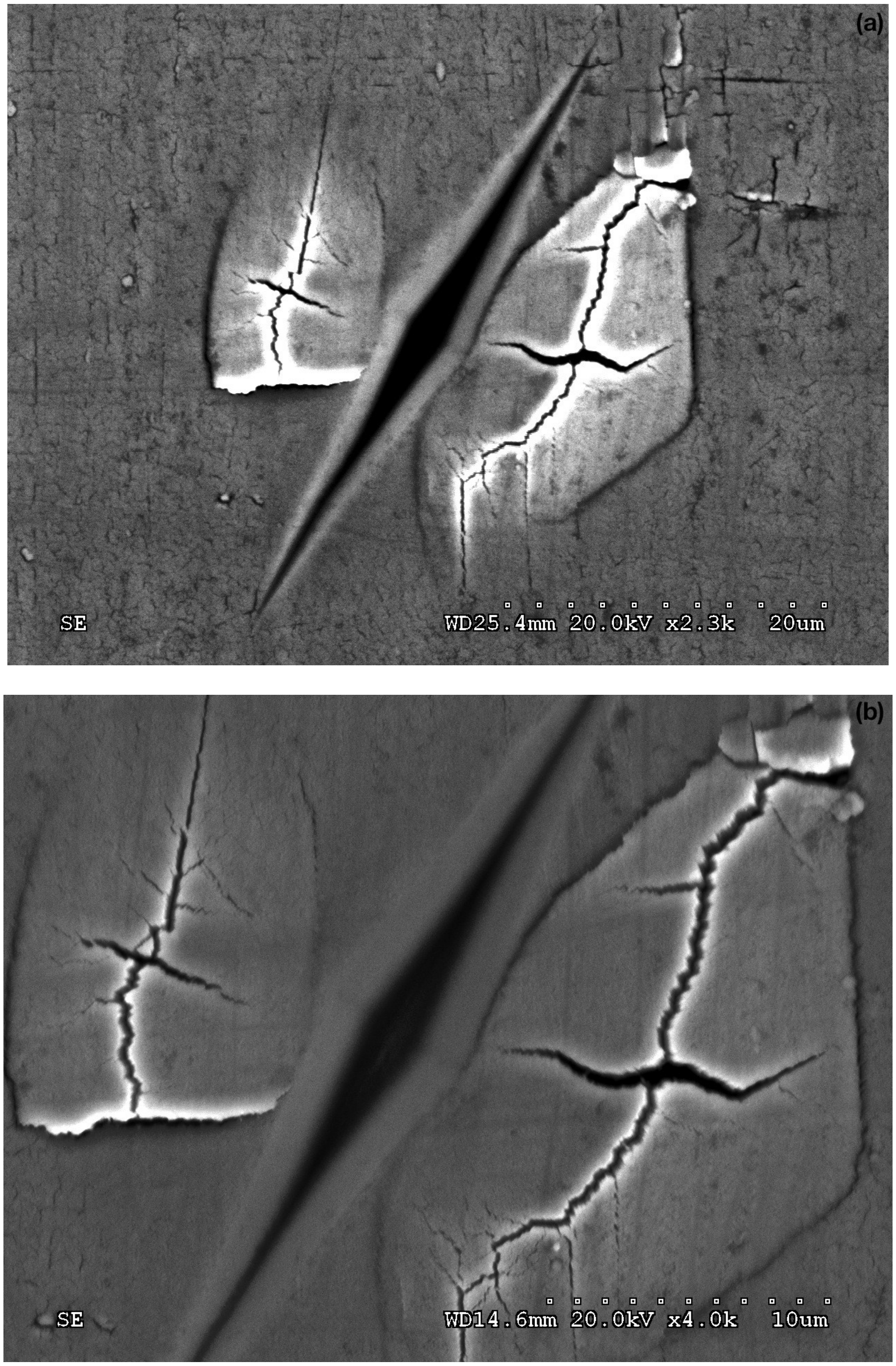

Figure 5.26: *Surface morphology of nc Ni film near 50* g_f *indentation after hydrogen charging at (a) low magnification and (b) buckling, spalling and radial cracks in film at high magnification.*

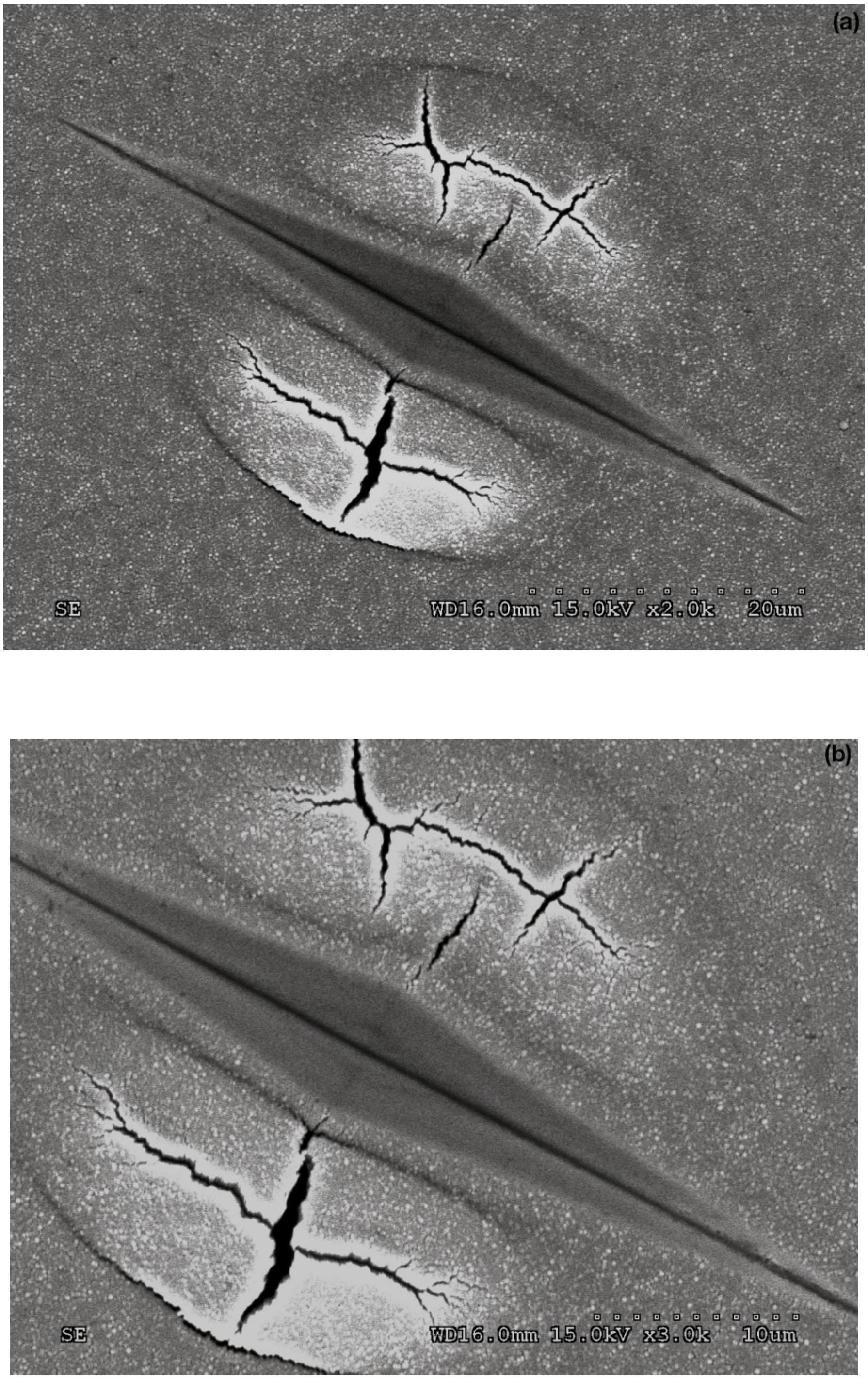

Figure 5.27: *Surface morphology of nc Ni film near 100 g_f indentation after hydrogen charging at (a) low magnification and (b) buckling, spalling and radial cracks in film at high magnification.*

The failure mechanism on indentation of the coating goes as follows:

Depending on indenter geometry, a ring, picture frame or radial crack occurs in the film as the indenter penetrates the film in the first stage. As applied load is increased in the second stage, an increase in crack opening is observed, which leads to delamination or buckling of the film. In the third stage, secondary through thickness cracks form a partial of full coating spallation occurs, depending on the flaw size distribution on the surface.

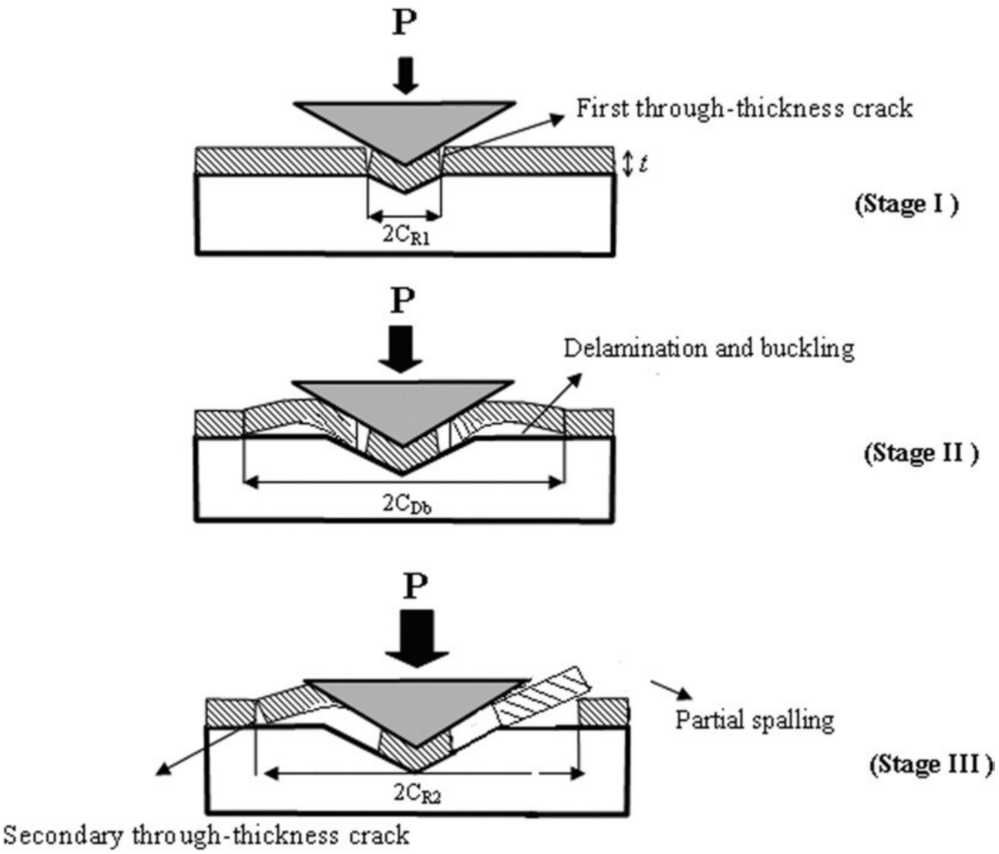

Figure 5.28: *Schematic of different stages of indentation-induced fracture for a brittle coating on a hard substrate* [47].

Fig. 5.28 represents this mechanism in the form of a schematic. The mechanism observed for the failure of hydrogen-charged nc Ni films is identical to one proposed by Li et al [48] and modified by Chen [47] for brittle coatings on a hard surface. This indicates that the ductile nc Ni coating is embrittled in the presence of hydrogen and fails on indentation due to its limited ability to deform plastically. Dislocation emission is limited due to small grain size, thus inducing embrittlement. This is not so in the bulk Ni that possesses a large grain size and ductile deformation takes place. In fact, the evidence for bulk Ni shows that enhanced plastic deformation takes place due to the presence of hydrogen. Obviously, in this case the near surface layer is affected by the hydrogen is narrow and HE does not occur.

The remarkable brittle fractures can be attributed to the very high density ratio of grain boundaries and triple junctions to material volume in the nc film, as compared to the bulk Ni. The results corroborate the concept of hydrogen adsorption in critical preferential places like triple points and grain boundaries.

CHAPTER 6

CONCLUSION

The corrosion and Hydrogen Embrittlement behavior of sputter-deposited nc Ni coatings has been compared with that of bulk Ni. The corrosion behavior is compared in 3.5 % NaCl and 0.1 N H_2SO_4 solutions.

Bulk Ni samples exhibited mild passivation in 3.5 % NaCl solution, whereas nc Ni films showed strong passivation and corrosion resistance. The higher grain boundary density in nc films could accelerate the formation of a strong and continuous passive layer and in turn, increase the corrosion resistance.

In 0.1 N H_2SO_4 solution, both bulk and nc Ni showed active behavior. However, nc Ni films corroded at a higher rate than its bulk counterpart. This is due to the absence of passivation process and the presence of high number of grain boundaries, which act as a catalyst to the hydrogen reduction reaction and increase the corrosion rate.

Nanocrystalline materials are expected to provide a generally higher corrosion rate due to a high density of grain boundaries. However, the advantage or disadvantage of these materials depends on whether the material can form a passive film in the environment or not.

Effect of hydrogen was also examined for bulk and nc Ni. Electrochemical charging of hydrogen yielded a small increase in hardness and may have caused hydrogen induced slip dislocation in bulk Ni. However, no cracking was observed at indent. The effect of hydrogen on nc Ni was adverse. Brittle failure of film was observed for 25, 50 and 100 g_f loads, characterized by buckling and spallation of the film. This is attributed to the limited ability of nc Ni to deform plastically by dislocation emission and motion.

REFERENCES

[1] G. P. K. A. U. Erb, Electrodeposited Nanostructured Films and Coatings: Sythesis, Structure and Applications, *Nanostructured Films and Coatings*, (2000), 11-24.

[2] J. V. P. M. K. Bouslykhane, Tribological properties of Nickel-base nanocrystalline coatings sputter-deposited on austenitic stainless steel, *Tribology International*, 29(2) (1996), 169-173.

[3] Y. L. F. W. Li Liu, Influence of grain size in the corrosion behavior of a Ni-based superalloy nanocrystalline coating in NaCl acidic solution, *Electrochemica Acta*, 53 (2007), 2453-2462.

[4] M. L. Jr., Hydrogen Embrittlement of Metals: A Primer for the Failure Analyst, *Defence Technical Information Center*, 8 (2008).

[5] A. Barnoush, Hydrogen Embrittlement, Materials Science and Methods at Saarland University, (2007).

[6] W. B. W. M. J. M. P. Bley, Description of Microstructures in LIGA-Technology, *Microelectronic Engineering*, 13(1-4) (1991), 509-512.

[7] R. Parkinson, Properties and applications of electroless nickel, *Nickel Development Institute,*.(1997).

[8] C. Cutler, Nickel, Nickel Everywhere, *Nickel Development Institute*, (1998).

[9] Corrosion Costs and Preventative Strategies in the United States, *NACE*, (2002).

[10] H. Gleiter, Nanocrystalline Materials, Advanced Structural and Functional Materials, *Springer Berlin Heidelberg,* (1991).

[11] U. E. I. Brooks, Hardness of electrodeposited microcrystalline and nanocrystalline γ-phase Zn-Ni alloys, 26 (2001).

[12] H. C. S.C. Tjong,Nanocrystalline materials and coatings, *Materials Science and*

Engineering: R: Reports, 45 (2004), 1-88.

[13] G. P. U. E. C. Cheung, Synthesis of nanocrystalline permalloy by electrodeposition, *Materials Letters*, 31(6) (1994), 135-138.

[14] H. V. S. S. S. K.S. Kumar, Mechanical behavior of nanocrystalline metals and alloys, *Acta Materilialia*, 51 (2003), 5743-5774.

[15] G. P. B. S. K. A. U. Erb, Electrodeposited v. Consolidated Nanocrystals: Differences and Similarities, *Acta Metallurgica*, 9 (1997), 261-270.

[16] S. Kim, "Corrosion Properties of Nanocrystalline Ni and Co Deposits," ProQuest Dissertations and Teses, (2004).

[17] W. Grove, On the Electro-chemical Polarity of Gases, Philosophical Transactions of the Royal Society London, 142(1) (1852).

[18] R. Bunshan, Handbook of Deposition Technologies for Films and Coatings, *Noyes Publications*, (1994).

[19] A. M. D.S. Rickerby, Advanced Surface Coatings: A Handbook of Surface Engineering, *Chapman and Hall*, (1991).

[20] "What is Sputtering," AJA International, Inc, [Online]. Available: http://www.ajaint.com/whatis.htm. [Accessed 05 February 2013].

[21] K. Y. A. O. T. D. T.. T. T. K. K. H. K. Y. Mikami, Effect of DC bias voltage on the deposition rate for Ni thin folms by RF-DC coupled unbalanced-magnetron sputtering, 133-134,(2000), 295-300.

[22] C. Q. J. R. C. Z. L. Gou, SiC film deposition by DC magnetron sputtering, vol. 345, (1999), 42-44.

[23] A. A. M. C. B.G Priyadarshani, Structural and morphological investigations,46, (2011), 2860-2873.

[24] R. M. J. W. P.L. Gai, Structural variations in nanocrystalline nickel, 74(9) (2002), 2860-2873.

[25] R. H. A. M. J. W. R. Mitra, Effect of process variables on the structure, residual

stress, and hardness of sputtered nanocrystalline nickel films, 16(4) (2001), 1010-1027.

[26] D. Landolt, Corrosion and Surface Chemistry of Metals, EPFL Press, (2007).

[27] G. Cragnolinio, Corrosion Fundamentals and Characterization Technique, *Woodhead Publishing Limited*, (2008).

[28] C. Huang, "Synthesis and Characterization of Nickel and Nickel Hydroxide Nanopowders," UNT Digital Library, [Online]. Available: http://digital.library.unt.edu/ark:/67531/metadc86874/. [Accessed 22 February 2013].

[29] M. S. B. J. C.G Telfer, Particle concentration and size effects on the erosion-corrosion of pure metals in aqueous slurries, *Tribology International,* 53 (2012), 35-44.

[30] J. Z. Y. G. Q. X. L. H. T. X. L. Wang, Grain size effect in corrosion behavior of electrodeposited nanocrystalline Ni coatings in alkaline solution, *Scripta Materialia,* 55 (2006) 657-660.

[31] J.-S. L. Q. J. L.-Y. Qin, Effect of grain size on corrosion behavior of electrodeposited bulk nanocrystalline Ni, *Transactions of Nonferrous Metals Society of China,* 20 (2010), 82-89.

[32] R. L. A. S. U. E. G. P. K. A. R. Rofagha, A Comparison Of The Corrosion Behaviour Of Nanocrystalline And Normal Crystalline Nickel," in *Materials Research Symposium Proceeding 283, 751* (1992).

[33] R. B. R.Mishra, Effect of nanocrystalline grain size on the electrochemical and corrosion behavior of nickel, *Corrosion Science,* 46 (2004), 3019-3029.

[34] S. K. W. G. L. O. L. S. D. Y. Pauleau, Structure and physical properties of nickel films deposited by microwave plasma-assisted cathodic sputtering, *Journal of Physics D: Applied Physics,* 39 (2006), 2803-2808.

[35] T. M. A. P. C. Borchers, Effect of hydrogen on the mechanical properties of stainless steel," *Advanced Engineering Materials ,* 10(1-2) (2008), 11-23.

[36] H. Liu, Hydrogen assisted intergranular cracking in steels," *Engineering Fracture Mechanics,* 78 (2011), 2563-2571.

[37] S. K. D. Koss, The effect of stress state on the hydrogen embrittlement of nickel, *Acta Metallurgica,* 34 (1986), 55-61.

[38] C. M. Jr., Hydrogen-induced intergranular fracture of steels," *Engineering Fracture Mechanics,* 68 (2011), 773-788.

[39] H. B. I.M. Robertson, An HVEM study of hydrogen effects on the deformation and fracture of nickel, *Acta Metallurgica,* 34 (1986), 353-366.

[40] P. S. H.K. Birnbaum, Hydrogen-enhanced localized plasticity--a mechanism for hydrogen-related fracture," *Materials Science and Engineering A,* 176 (1994), 191-202.

[41] J. C. J. B. C. S. B. P. X. F. A. Oudriss, The Diffusion and trapping of hydrogen along the grain boundaries in polycrystalline nickel, *Scripta Materialia,* 66 (2012), 37-40.

[42] A. C. A.M. Brass, Accelerated diffusion of hydrogen along grain boundaries in nickel," *Acta Metallurgical,*44(9) (1996), 3823-3831.

[43] G. P. K. A. A. E.-S. U. E. D.M. Doyle, The influence of intercrystalline defects on hydrogen activity and transport in nickel, *Acta Metallurgica et Materialia,* 43(8) (1995), 3027-3033.

[44] X. H. C. M. R. K. D.R. Arantes, "Hydrogen diffusion and permeation in micro- and nanocrystalline nickel," *Acta Metallurgica et Materialia,*41(11) (1993), 3215-3222.

[45] D. D. A. E.-S. U. E. K. A. G. Palumbo, Intercrystalline hydrogen transport in nanocrystalline nickel, *Scripta Metallurgia et Materilia,* 25(3) (1991), 679-684.

[46] A. G. J. C. X. F. C. Savall, Influence of deposition parameters on microstructure and contamination of electrodeposited nickel coatings from additive-free sulphamate bath, *Surface and Coatings Technology*, 206 (2012),.4394-4402.

[47] J. Chen, Indentation-based methods to assess fracture toughness for thin coatings," *Journal of Physics D: Applied Physics,* 45 (2012).

[48] D. D. B. B. X. Li, Fracture Mechanisms of Thin FIlm Amorphous Carbon Films in Nanoindentation, *Acta Materialia,* 45(11) (1997),4453-4461.

[49] U. Erb, Electrodeposited Nanocrystals: Synthesis, Structure, Properties and Future

Applications, *Canadian Metallurgical Quarterly*, 34(3) (1995), 275-280.

[50] L. W. M. Troyon, Influence of saccharin on the structure and corrosion resistance of electrodeposited Cu/Ni multilayers, *Applied Surface Science*,103 (1996), 517-523.

[51] G. R. J.O.M. Borkis, Fundamental Aspects of Electrocrystallization, *Plenum Press*, (1967).

[52] M. P. A. F. S. S. N. F. W. M. J.K. Luo, Effects of Process Conditions on Properties of Electroplated Ni, Journal of the Electrochemical Society, 153(10) (2006), 155-160.

[53] A. A. A.M. Rashidi, "Effect of Electroplating Parameters on Microstructure of Nanocrystalline Nickel Coatings, *Journal of Materials Science and Technology*, 26(1) (2010), 82-86.

[54] A. A. A.M. Rashidi, Effect of Electroplating Parameters on Microstructure of Nanocrystalline Nickel Coatings, *Journal of Materials Science and Technology*, 26(1) (2010), 82-86.

[55] I. E. M. F. G. M. J. Amblard, Inhibition and nickel electrocrystallization, *Journal of Applied Electrochemistry*, 9 (1979), 233-242.

[56] J. C. X. F. E. C. L. P. C. A. C. S. A Godon, Characterization of electrodeposited nickel coatings from sulphamate electrolyte without additive, *Materials Characterization*, 62 (2011), 164-173.

[57] A. T. J. K. S. G. J. M. E.A. Marquis, Effects of current density on the structure of Ni and Ni–Mn electrodeposits, *Journal of Applied Electrochemistry*, 36(6) (2006), 669-676.

[58] C. S. S. Ruan, Mesoscale structure and segregation in electrodeposited nanocrystalline alloys, *Scripta Materialia*, 59 (2008), 1218-1221.

[59] P. F. C. S. B.Y.C. Wu, Nanostructured Ni-Co Alloys with Tailorable Grain Size and Twin Density,*Metallurgical and Materials Transactions A*, 36A(7) (2005), 1927-1936.

[60] K. S. R. Weil, The structures of electrodeposits: Their characterization and the properties they affect, *Materials Characterization*, 28(2) (1992), 103-112 .

[61] P. M. M. S. A.A. Rasmussen, Influence of 1,3,6 napthalene trisulfonic acid on microstructure and hardness in electrodeposited Ni layers,*Plating and Surface Finishing*, 89(10) (2002), 46-49.

[62] H. Srivastava, Microstructure of Nickel Electrodeposited from a Nickel Sulfamate/Formamide Bath,*Metal Finishing*, 93(5) (1995), 20-27.

[63] L. G. R. J. O. S. R. Ramanauskas, Structural and corrosion characteristics of pulse plated zinc coatings, *Electrochemica Acta*, 53(4) (2006),1801-1810.

[64] C. P. d. L. F. W. P. Herrasti, The corrosion behaviour of nanograined metals and alloys(•)," *Revista de Metalurgia,* 48(5) (2012), 377-394.

[65] A. D. G. E. J. Peŝiĉkaa, Free dislocations and boundary dislocations in tempered martensite ferritic steels," *Materials Science and Engineering: A,* 387–389 (2004), 176-180.

[66] W. R. H. Vehoff, Gaseous hydrogen embrittlement in FeSi- and Ni-single crystals," *Acta Metallurgica,* 31(11) (1983), 1781-1793.

BIOGRAPHICAL INFORMATION

Tapas Desai was born in Rajkot, India. He completed his Bachelor’s degree in Metallurgical and Materials Engineering from Gujarat University, India in 2011. He then went on to pursue a Master’s degree in Materials Science & Engineering at the University of Texas at Arlington, where he studied the corrosion and hydrogen embrittlement properties of nanocrystalline Nickel with the support and guidance of Dr. E. I. Meletis.